The role of oxygen reduction reaction in determining pit stability of FeCr alloys

*Y. Wang[1], M.-F. Ng [2], T.L-Tan[2], D.J. Blackwood[1] **

[1]Department of Materials Science and Engineering, National University of Singapore, 9 Engineering Drive 1, Singapore 117576

[2]Institute of High Performance Computing, Agency for Science, Technology and Research, 1 Fusionopolis Way, #16-16 Connexis, Singapore 138632, Singapore

Abstract

Pitting corrosion is one of the most dangerous forms of corrosion, leading to sudden catastrophic failures in engineering system. Once initiated, pit propagation rates are largely dependent on the magnitude of the supporting cathodic current available from the oxygen reduction reaction (ORR) occurring on the external passive film. Here the ORR kinetics on conventional and high Cr content FeCr alloys made by arc-melter were investigated by experimental and computational methods. DFT calculations suggested that the overpotentials for the ORR on FeCr oxides are in the order Cr_2O_3 > Fe_3O_4 > Fe_2O_3 > $FeCr_2O_4$, which was experimentally confirmed on the FeCr alloys by rotating disc electrode experiments in both O_2 saturated 0.1 M NaOH and 3.5 wt% NaCl. Koutecký-Levich analysis demonstrated that ORR follows a 4-electron pathway on all surfaces investigated. Moreover, the investigation of the Pourbaix diagrams of FeCr revealed that at potentials where pitting corrosion initiates the main constituents of the passive films should be a mixture of Fe_2O_3 and Cr_2O_3, rather than $FeCr_2O_4$, which is proved to be a good ORR catalyst. The results support the postulation that one role Cr additions play in the prevention of pitting corrosion is to suppress the ORR reaction.

Key words: *A: FeCr alloys; B: rotating disc electrode ; B: modelling studies; C: pitting corrosion; C: oxygen reduction.*

* **Corresponding Author:** msedjb@nus.edu.sg (Daniel John Blackwood), Tel: (65) 6516-6289, Fax: (65) 6776-3604

Graphical Abstract

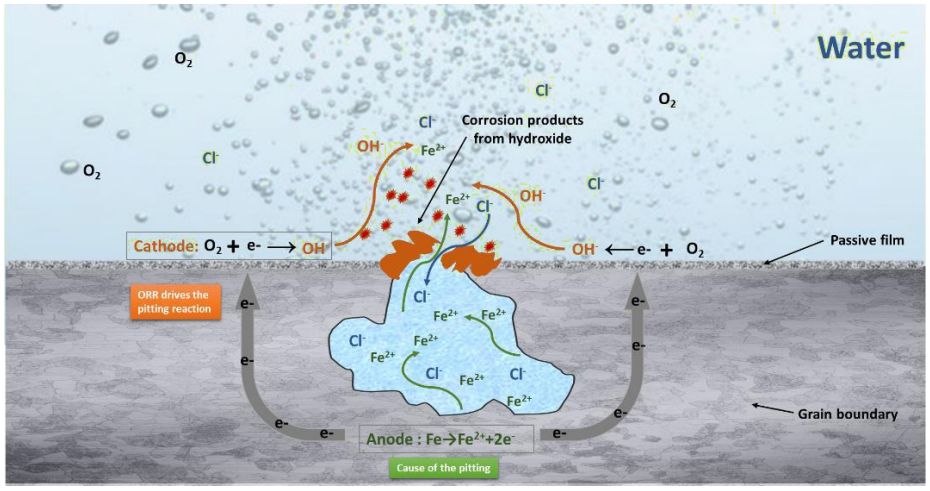

1 Introduction

Localized pitting corrosion of FeCr alloys, such as stainless steels occurs when there is a discreet failure in the protective passive film, usually associated with attack by aggressive ions such as chloride [1, 2]. Because the majority of the surface is not affected, pitting is hard to detect, making it significantly more of a concern to industry than general uniform corrosion. The pit initiation process is still not well understood [3-8], but once the protective oxide has been breached pit propagation occurs via an electrochemical process: the metal surface exposed within the pit acts as the anode generating metallic ions, while the remaining oxide outside of the pit acts as the cathode for the supporting oxygen reduction reaction (ORR). For example:

$$M \rightarrow M^{n+} + ne^- \quad (1)$$

$$O_2 + 2H_2O + 4e^- \rightarrow 4OH^- \quad (2)$$

Under open-circuit free corrosion conditions, the rate of the electron generation by the anodic corrosion reaction has to be matched by the rate of the electrons are consumed by the cathodic oxygen reduction reaction; therefore, the corrosion rate is often limited by the rate of its supporting cathodic reaction. As early as 1968, Horvath & Uhlig recognized that how fast a pit grows is dependent on the cathodic current available from oxygen reduction reaction [9].

Once a pit initiates it can either grow and propagate into the metal or the passive film may reform causing the pit to die [10]. Whether the pit lives or dies depends on a range of environmental factors, one of the most important of which is how quickly the pH of the occluded pit solution falls to a level that the passive film oxides would become soluble. That is to say, pit survival depends on a race between the rates of acidification of the occluded pit solution and the regrowth of the damage passive film. Acidification within the pit solution occurs from a combination of hydrolysis

of metallic ions and the migration of aggressive ions into the pit to maintain charge neutralization in the well know crevice corrosion mechanism [11]. Therefore, the rate of acidification is directly related to the rate of metal dissolution at the pit walls, which in turn is restricted by available cathodic current provided by the ORR occurring on the passive film outside of the pit. Consequently, it follows that a reduction in the kinetics of the ORR on the passive film will favour repassivation, pit death, implying that the chemical nature of the passive film is important in determining an alloy's resistance to pitting corrosion. Note that the ORR is known to proceed via two possible pathways: a 2-electron pathway where the dissolved oxygen is partially reduced to hydrogen peroxide; and a 4-eletrcon pathway where dissolved O_2 is completely reduced to water or hydroxide ions.

For stainless steels the passive film is usually a combination of iron (Fe) and chromium (Cr) oxides; for example, chromia (Cr_2O_3) and hematite (Fe_2O_3) and their hydroxylated forms $Cr(OH)_3$ and $Fe(OH)_2$/$Fe(OH)_3$ [12-16]. Indeed, numerous studies [12, 17-21], have been conducted to obtain a thorough understanding of the oxygen reduction reaction on stainless steel come out with similar conclusions revealing the important roles of oxides/ hydroxide of the main components, Fe and Cr, in stainless steel. In our previous work we used density functional theory + U calculations to investigate ORR activity on the Cr_2O_3 and Fe_2O_3 passive layers with (0001) surface [22]. The findings were that the overpotentials of oxygen reduction on the hydroxide-terminated Cr_2O_3 layer are much higher than that of the Fe_2O_3 layer, suggesting that the chromia surface will have poor ORR kinetics and that likely contributes to the well-known fact that increased Cr levels improves the pitting resistance of stainless steels. In the present work, we aim to verify the findings of our earlier DFT models by experimentally investigating the kinetics of the ORR on pure Fe and pure

Cr as well as a range of FeCr alloys via the rotating disc electrode (RDE) technique, to determine if the ORR kinetics can indeed be correlated to the FeCr resistance to pitting corrosion. Although pitting corrosion tests are normally conducted in saline solutions, pure Fe and low Cr alloys undergo rapid corrosion in such solutions, as such the ORR investigations were mainly conducted in 0.1 M NaOH, with only a few tests in 3.5 wt.% NaCl on selected high Cr samples.

2 Experimental

The FeCr alloy specimens were prepared by arc melting from different ratios of 99.98% pure iron (Sigma-Aldrich) and 99.9% pure chromium (American elements) under an Argon atmosphere. For weight loss experiments, referring to ASTM Standard G48–11 [23], the cast samples were cut into uniform rectangular plates (20 mm × 10 mm × 2 mm) and polished with 240 grit silicon carbide paper. The specimens were placed on glass cradles to minimize crevice corrosion and immersed in 70 ml $FeCl_3$ solution (6% $FeCl_3$ by mass) at room temperature (23.3-23.6 °C) for 72 h. Then, the specimens were taken out from the solution and rinsed and scrubbed with a nylon bristle brush under running water to remove corrosion products on the surface. After dipping in acetone and cleaning with ultrasonication for 10 minutes to remove corrosion products from deep pits, the specimens were dry by air. Photographs showing the sample situations with measurements of the length, width, thickness and weight of each specimen were recorded before and after the weight loss tests.

For the electrochemical experiments casted rods with a diameter of 8 mm were cut and manufactured into rotating disc electrodes with a diameter of 5 mm and embedded in a polytetrafluoroethylene (PTFE) shroud directly without any further heat treatments. The

electrodes were ground consecutively with 240 grit, 400 grit, 600 grit, 1200 grit, 2400 grit and 4000 grit SiC paper and were further polished with alumina down to 1 micron. After polishing, the disc electrode was attached to a Pine Research Instrumentation rotator (model: AFMSRXE, serial:1591) that has very fine control of the electrode's rotation rate.

All electrochemical tests were conducted with a Metrohm electrochemical workstation (PGSTAT302N with FRA32M Module). The electrolyte was 0.1 M NaOH aqueous solution, which was used to prevent rapid corrosion of the pure and low Cr alloys when positive potentials were applied. A standard RDE cell containing the electrolyte as described above was used for the ORR tests. A dual gas inlet was mounted in one side port to provide either a de-aerated (Argon) or a saturated oxygen atmosphere, while platinum mesh was used as the counter electrode and a Hg/HgO (0.1 M NaOH) electrode (0.165 V vs NHE / 0.932 V vs RHE [24]) with the Luggin tube to minimize uncompensated resistance was chosen as the reference electrode. However, all results presented have been converted to the reversible hydrogen electrode (RHE) scale. The RDE was freshly polished before each test and polarized at -1.65 V vs. Hg/HgO (0.1M NaOH) for 10 min to reduce air-formed oxides. The potential was next swept from -1.3 V to 0.3 V vs. Hg/HgO (0.1M NaOH) at a rate of 5mV s^{-1}, where it was held for 10 min to allow oxide film growth to reach a steady state. The reverse polarization curves were then recorded by the linear sweep voltammetry at 5 mV s^{-1} with a rotation rate of the electrode ranging from 0 to 2500 rpm. The onset potential (vs RHE) for the ORR was defined as the potential at which the cathodic current densities reached −0.1 mA cm^{-2}, commonly used to indicate an electrode's catalytic performance [25, 26]. The experimental overpotential for ORR was then defined as

$$\text{Experimental overpotential} = 1.23\ \text{V} - \text{Onset potential (V vs RHE)} \quad (3)$$

It is important to note that this is different from the overpotential calculated from DFT analysis, which is the related to the calculated reaction free energy from the equilibrium potential and the reaction potential of the ORR process [22]. RDE experiments were also conducted in 3.5 wt.% NaCl on selected high Cr samples to confirm the trends observed in 0.1 M NaOH.

Cyclic potentiodynamic polarization (CPP) measurements were conducted in a typical three-electrode system with the FeCr alloy specimens as the working electrode, a saturated calomel electrode (SCE) as the reference electrode and a graphite rod as the counter electrode. The tests were carried out in 3.5 (wt.%) NaCl aqueous solution (pH 6.3), which was de-aerated with Argon for 30 min first, after which the open circuit potential (OCP) was recorded for a further 30 min to achieve an approximately stable potential before polarization test were conducted. Each specimen was scanned potentiodynamically at a rate of 0.1667 mV s^{-1} (10 mV min^{-1}) from the OCP until the current density reached an upper threshold limit of 0.1 mA cm^{-2}, at which point the scan direction was reversed.

A Zeiss Supra 40 Scanning electron microscopy (SEM) with energy-dispersive X-ray spectroscopy (EDS) was employed for the analysis of the surface and composition of the alloys. A Raman spectrometer (Horiba LabRAM HR Evolution, with an argon-ion 514 nm laser operating at 100 mW) and a Bruker D8 Advance thin film X-ray diffraction (using Cu Kα radiation, in the 2θ range of 5° to 80°, using a step size of 0.02° and time per step of 1 s) were used to identify the structure of the compounds formed on the surface of the alloys. A Bruker D8 Advance Powder X-ray diffraction (using a step size of 0.01° and time per step of 0.2 s in the 2θ range of 5° to 100°) was chosen for the crystal structural characterization of the cast alloys.

DFT calculations were performed using the Perdew, Burke, and Ernzerhof (PBE) exchange-correlation functional [27] implemented in Vienna Ab-initio Simulation Package (version 5.4) [28]. The projector augmented wave (PAW) method [29] was used for describing the core-valence interaction. The rotationally invariant approach using the U parameters was utilized [30, 31] to correct the effects from the strongly correlated electrons in transition metal ions. The adopted U values for Fe and Cr were 4.3 and 3.7, respectively, taken from Ng et al [22]. The kinetic energy cut-off for the plane-wave expansion was set at 520 eV. A 4×4×1 Monkhorst Pack sampling *k*-point grid was used. During geometry optimizations, the bottom layer of atoms together with the bottom OH groups were frozen, while the rest of the ions were fully relaxed until the total energy and absolute value of the forces acting on each atom were less than 1×10^{-6} eV and 1×10^{-2} eV $Å^{-1}$, respectively. A vacuum layer of at least 15 Å and dipole corrections were applied. The Gibb free energy (ΔG) diagrams were calculated using the equation:

$$\Delta G = \Delta E + \Delta ZPE - T\Delta S + e\phi \qquad (4)$$

where ΔE is the DFT reaction energy, ΔZPE is the change of zero-point energy, T is temperature; ΔS is the change of entropy; and ϕ is the external applied potential. ZPE corrections were obtained from the vibrational frequency calculations. The values of entropic energy terms (TS) for H_2 and H_2O were taken from standard thermodynamics table. Since O_2 molecule was not described well by DFT [32], its DFT energy was derived from DFT energies of H_2 and H_2O, and the formation free energy of H_2O determined from experiment. Details of the equations describing the 4-electron associative and dissociative ORR mechanisms are shown in Figure S3 in the Supporting Information.

Pourbaix diagrams were obtained from an online programme called *Materials Project* [33-35] through a methodology utilizing experimentally measured free energies of aqueous ions and the calculated DFT energies for solid phases. A molar concentration of 10^{-6} M was set for the soluble species.

3 Results & Discussion

Figure 1 shows SEM-EDS images for the Fe35Cr65 alloy, which reveals that the Fe and Cr are distributed evenly in the cast alloy. The other composition alloys show a similar evenly elemental distribution. The chemical composition of the FeCr alloys is estimated from the EDX results based on a mean value of at least five different sites of the tested alloy. The content of Cr in the EDX results are consistent with the Fe-Cr ratios used for smelting with negligible differences (Figure 1d).

The XRD patterns of the as-prepared FeCr alloys with Cr content in the range of 15–75 wt.% are presented in Figure 2. The spectra consist of broad peaks that reveal the polycrystalline nature of the alloys produced by arc melting. The main diffraction peaks are well matched with cubic Cr ((JCPDS No. 00-006-0694), cubic Fe ((JCPDS No. 00-001-1262), and cubic FeCr alloy ((JCPDS No. 00-034-0396). This suggests that the primary phase of the FeCr alloys is identified as a body-centred-cubic (BCC) phase, with BCC fundamental reflections [(110), (200), (211) and (220)]. Due to the similarity in size and structure of Fe and Cr, the lattice misfit is small. No other phase than the BCC is observed at any composition in the XRD patterns.

The polarization curves of Fe and Cr in 0.1 M NaOH saturated with O_2 for both positive (forward) and negative (reverse) scan directions are presented in Figure 3. For the Fe electrode, the limiting current densities for the forward and reverse scans are very similar at all rotation rates (Figure 3e), indicating similar reaction pathways on a bare/partially oxide covered and a fully oxide covered Fe surfaces [12, 36]. However, the onset potential for ORR is more negative for the reverse sweep than its forward counterpart, indicating that ORR requires a larger overpotential on the fully oxide covered surface, which is consistent with previous reports [37]. In the case of the pure Cr disc electrode, well-defined diffusion limiting currents are observed from the forward scans (Figure 3c). In contrast, for the reverse scans the ORR current densities were almost independent of rotation rates, being up to an order of magnitude smaller than that observed in the respective forward scans, with no diffusion limiting current density being reached before the onset of the hydrogen evolution reaction (Figure 3d).

Since the ORR generates hydroxide ions, it is possible that this causes a local pH increase at the electrodes surface. For an RDE any change in the surface OH^- concentration ($C_{surf(OH^-)}$) from its bulk value ($C_{bulk(OH^-)}$) can be estimated from the ORR limiting current density via Equation (5), with the number of electrons generated per hydroxide ion (n) being unity and the thickness of the diffusion layer (δ) of a rotating system is given by Equation (6).

$$C_{surf(OH^-)} - C_{bulk(OH^-)} = I_{lim}\delta/(nFD_{(OH^-)}) \quad (5)$$

$$\delta = 1.61\, D_{(OH^-}{}^{1/3}\nu^{1/6}\omega^{-1/2} \quad (6)$$

where D_{OH^-} is the diffusion coefficient for hydroxide ions (5.7×10^{-5} cm^2 s^{-1}[38]), F is the Faraday constant (96485 C mol^{-1}), ν is the kinematic viscosity (1.1×10^{-2} cm^2 s^{-1}[39]), ω is the angular rotation rate of the electrode (rad s^{-1}). Although the pH change can be significant in

neutral solutions, calculations showed that in 0.1 M NaOH even for the largest limiting ORR current densities recorded in Figure 3 any increase in the surface concentration of OH^- ions would be negligible, at most changing the pH in the second decimal place.

Figures 4a and 4b show comparisons between the pure metal ORR curves collected in the forward and reverse directions at 1500 rpm, respectively. For the forward scans the onset potentials are similar on the two metals, although the limiting current density is slightly lower with the Cr electrode that may suggest that a higher degree of the 2-electron transfer pathway occurs on its surface than its Fe counterpart. For the reverse scans, Figure 4b shows that the ORR onset potential is significantly more negative on the Cr electrode (0.089 V vs RHE) than its Fe counterpart (0.299 V vs RHE) and the limiting current density is an order of magnitude smaller on the Cr electron than the Fe one. This indicates that the oxide-covered Cr surface is a very poor ORR electrode, requiring a much larger overpotential than its oxide-covered Fe counterpart (Figure 4b). Thus, the experimental results are in excellent agreement with our previous work [22] on DFT study of oxygen reduction reaction on chromia and hematite, which predicted Fe_2O_3 to be a far more catalytic surface for ORR than Cr_2O_3, suggesting a higher proportion of Cr_2O_3 in the passive film helps inhibit the oxygen reduction on the surface of stainless steels and thereby help delay the acidification of solution in the occluded pits.

The number of electrons involved in the mixed diffusion (mass transport) and kinetic controlled oxygen reduction reaction was further investigated by the Koutecký–Levich equation [12]:

$$1/(i-i_0) = 1/i_k+1/i_{Levich} = 1/i_k + B^{-1} N_r^{-1/2} \quad (7)$$

$$B = 0.2\, nFCD^{2/3} \nu^{-1/6} \quad (8)$$

where i is the measured current density in solutions saturated with O_2; i_0 the residual current density measured in solutions deoxygenated with Ar; i_k is kinetic current density from the Faradaic electrochemical reactions and i_{Levich} is the mass transport limiting current density; n is the number for transferred-electrons per oxygen molecule; D is the oxygen diffusion coefficient (1.9×10^{-5} cm^2 s^{-1}); ν is the kinematic viscosity (1.1×10^{-2} cm^2 s^{-1}); C is the bulk concentration of dissolved oxygen in the electrolyte (1.22×10^{-6} mol cm^{-3}) [40] and N_r is the disc electrode's revolution rotation rate (rpm). Note that the 0.2 constant in Equation (8) converts to 0.62 when the electrode's rotation rate is expressed in angular rotation rate (rad s^{-1}).

The Koutecký–Levich plots in Figure 5 were obtained by plotting $1/(i-i_0)$ against $_rN^{-1/2}$ at three different potentials, -0.018 V, -0.068 V and -0.118 V vs RHE (-0.95 V, -1.0 V and -1.05 V, vs. Hg/HgO (0.1M NaOH)), in the ORR potential range. Table 1 shows the fitting equations along with the effective number of electrons, "n" values, involved in the ORR pathway. For the Fe electrode the ORR limiting current densities are almost identical at the same potential, resulting in similar slopes from the Koutecký–Levich plots. The linear fitting results show that the ORR on the Fe surfaces (Figure 5a & 5b) predominately goes through the 4-electrons pathway, with the reverse scan (negative direction, Figure 5b) having a slightly higher n value, indicating that the fully oxide covered iron surface is slightly more favourable than the initial bare/partially oxidized Fe surface (Table 1). As to the Cr electrode, the Koutecký–Levich plots for forward scans reveal much lower n values than their Fe counterparts (Figure 5c), suggesting either a larger contribution from the 2-electron pathway (i.e. a reduction in the ORR proceeding by the 4-electron pathway) or that the initial Cr surface was partially coated by oxide that inhibited the ORR; note that the respective Pourbaix diagrams reveal that chrome oxides are

thermodynamically more stable (harder to electrochemically reduce) than iron oxides and thus less likely to have been completely removed by the initial 10 minute negative polarization at -1.65 V vs. Hg/HgO conducted at the beginning of the experiments. Figure 3d shows that the polarization curves from the reverse scans of Cr are virtually independent of the scan rates, therefore, the Koutecký–Levich analysis is not applicable to this case.

From the fitting results for the Koutecký–Levich plots and the n values displayed in Table 1, it can be inferred that the 4-electrons pathway dominates in the oxygen reduction on Fe and Cr electrodes. This justifies our choice of the 4-electron ORR pathway in our previous modelling work [22]. Furthermore, in that work we showed that at the equilibrium potential on OH-terminated Cr_2O_3 and Fe_2O_3 slabs, the Cr_2O_3 was calculated to have the higher overpotential, 2.78 V (vs. RHE), indicating it should exhibit a lower ORR activity than the Fe_2O_3, which was found to have a lower overpotential of 1.48 V (vs. RHE). The good consistency between experimental data and the computational modelling results demonstrates that DFT modelling is a potentially effective approach to understanding the ORR mechanism of the metals or alloys in corrosion science.

Figure 6a shows forward polarization curves for a series of FeCr alloys in O_2 saturated 0.1 M NaOH at a rotation rate of 1500 rpm. It can be seen that in terms of the ORR limiting current densities the FeCr alloys can be divided into two groups: the conventional (low) Cr content group including 15% Cr, 20% Cr and 25% Cr all show similar limiting current densities that are slightly below that of pure Fe; and the high Cr content group containing 50% Cr, 65% Cr and 75% Cr, which again show similar limiting current densities, but at lower values than their low

Cr counterparts. With respect to the onset potentials, these were almost independent of the rotation rates for low Cr content alloys. However, the onset potentials of high Cr content alloys moved in the positive direction (lower overpotential) as the rotation rate increased, which could be attributed to combined effects of the increased Cr_2O_3 in the film and the formation of $FeCr_2O_4$, the formation of the spinel having been reported to be promoted by an increase in the oxygen partial pressure [41] (Tables S1).

For the reverse scans, with fully formed oxides, the limiting current densities were almost independent of composition for Cr contents between 0% and 50%, but the onset potential ORR moved in the positive direction with increasing Cr content (Figure 6b & Table S2). This trend was unexpected, as if the passive film consisted of just a mixture of Fe_2O_3 and Cr_2O_3, one would have expected a negative shift in the onset potential with increasing Cr content. However, for Cr contents above 50% the ORR limiting current density declined significantly and the expected negative shift in the onset potential was observed (increasing ORR overpotential). As an aside it can also be seen from Figure 6b that for the reverse scans, hydrogen evolution is much more efficient on the pure Fe than that on any of the FeCr alloys.

Figures 6(c) & 6(d) demonstrate that the comparison of the forward and reverse polarization scans reveals that the low Cr and high Cr groups display completely opposite trends. On the one hand, for the low Cr group, the reverse scan, with a fully formed oxide film has better ORR activity, showing a slightly larger limiting current density and a more positive onset potential, than the forward scan with a bare or partially formed oxide film. On the other hand, for the high Cr group, it is the forward scan (bare or partially oxidized surface) that shows the better ORR

catalytic activity, since once the oxide is fully formed no limiting current density is observed due to the influence of chromia, on which the ORR kinetics is so poor that it does not become fully mass transport controlled prior to the onset of the hydrogen evolution reaction (Figure 6d).

Koutecky-Levich analysis was also conducted for the range of FeCr alloys during both their forward and reverse scans (Tables S3 & S4), which suggests the 4-electron pathway dominates in all cases; although the Koutecky-Levich analysis for the very high Cr content alloys on the reverse scans was unreliable as clear limiting current density plateau could not be discerned.

However, analysis of the ORR limiting current densities paints a slightly different story. Figure 7 shows a plot of the measured limiting current densities recorded at different rotation rates (100 rpm, 1500 rpm & 2500 rpm) for the forward (solid symbols) and reverse (open symbols) scans, against the alloy composition. Marked on the plot in Figure 7 are the theoretical limiting current densities expected for an oxygen saturated solution (dissolved oxygen concentration 1.22×10^{-6} mol cm^{-3} [40]) undergoing the 2 electron (dashed lines) and 4-electron (solid lines) pathways at the various rotations rates. It can be seen that if the Cr content does not exceed 50 wt.% the measured current density is close to that expected for the 4-electron pathway for both forward and reverse scans and this is also the case for higher Cr contents during the forward scans.

However, during the reverse scan, when the passive film is fully formed on the high Cr (>65 wt.%) containing alloys the ORR limiting current densities are more in line with the values expected for the 2-electron pathway, especially at high rotation rates. For example, the measured ORR limiting current density of Fe25Cr75 sample at 100 rpm is consistent with that expected for the 4-electron pathway, but at 1500 rpm the limiting current density is close to the value expected for the 2-electron pathway and does not increase significantly when the rotation rate is

increased to 2500 rpm (Figure 7). However, it will be explained later that the apparent switch from the 4-electron to the 2-electron pathway with increasing the Cr content is likely an illusion caused by a reduction in ratio of the catalytic $FeCr_2O_4$ to inhibitive Cr_2O_3 in the oxide film.

The ORR results from the oxide covered pure Fe and pure Cr agree with our earlier DFT calculations for Fe_2O_3 and Cr_2O_3. If the nature of the passive film on the FeCr alloys is simply a mixture of Fe_2O_3 and Cr_2O_3, one would expect a gradual decrease in ORR catalytic ability as the Cr content of the alloy increases. However, the ORR catalytic activity of the alloys containing up to 50% Cr was as good or better than pure Fe. For example, Figure 8 shows that at high rotation rates (>1500 rpm) the onset potential shifts in the positive direction (smaller experimental overpotential) as the Cr fraction increases to 50% and then shifts back in the negative direction as the Cr content further increase. A similar behaviour occurs at the lower rotation rate of 100 rpm, except the smallest experimental overpotential is observed in Fe35Cr65 alloy, as opposed to the Fe50Cr50 alloy at the higher rotation rates.

The most likely explanation for this behaviour is that the passive film on the FeCr alloys is not a simple mixture of Fe_2O_3 and Cr_2O_3. Indeed, Pourbaix diagrams obtained using the *Materials Project* suggests the appearance of $FeCr_2O_4$ in the passive film (Figure 9); as also proposed from experimental studies on stainless steels in borate solutions by Wijesinghe and Blackwood [42]. The passive films on the FeCr alloys were too thin to analyse by either XRD or Raman spectroscopy, but when the positive potential limit of the polarization scan was extended into the transpassive region (an extra 350 mV) a thick film became visible by the end test scanned from -1.3 V to 0.3 V vs. Hg/HgO (Figure S1). For the Fe35Cr65 alloy, XRD of this film revealed a

peak for two-theta at 35.5°, which could be assigned to $FeCr_2O_4$ (Figure S1c), and the Raman spectrum was consistent with the structure of a spinel in the literature [43, 44].

Table 2 summarizes the experimentally obtained ORR onset potentials from the reverse scans, along with the experimental overpotentials calculated via Equation (3) for the range of FeCr alloys. Table 2 also shows the possible thermodynamically stable constitutions of the alloys' passive films in 0.1 M NaOH at the ORR onset potentials, based on their calculated Pourbaix diagrams; the mole fraction of $FeCr_2O_4$ in the passive film is estimated by assuming the Fe:Cr ratio in the oxide remains the same as in the parent alloy and that the remainder of the passive film is either Fe_2O_3 or Cr_2O_3. It can be seen that as the content of $FeCr_2O_4$ increases the experimental ORR overpotentials generally decreases, indicating that $FeCr_2O_4$ a good ORR catalyst. This is consistent with the work of Boudjemaa et al [45] who have shown that $FeCr_2O_4$ is a good photocatalyst for the water–gas shift reaction. The apparent discrepancy that the lowest experimental overpotential does not occur with the Fe35Cr65 alloy, which is predicated to have a pure $FeCr_2O_4$ passive film, but with the Fe50Cr50 alloy can be explained by the well reported Cr enrichment of passive films on FeCr alloys [46-48]. Furthermore, it is recognized that the $FeCr_2O_4$ is probably only one of series of $Fe_xCr_{3-x}O_4$ intermediates.

The formation of a mixture of Cr_2O_3 (poor ORR catalyst) and $FeCr_2O_4$ (good catalyst) also explains why the ORR reaction appears to follow the two-electrons pathway on passive films of the high Cr containing alloys (Figure 7); i.e. only the $FeCr_2O_4$ regions contribute to the measured ORR limiting current density, with the reduction in effective surface area (with more Cr_2O_3 incorporated in the film) giving the false impression of a switch from the 4-electrons to the 2-

electrons pathway. This phenomenon does not occur with the low Cr containing alloys as iron oxides are better ORR catalysts.

However, the presence of a mixed Cr_2O_3 and $FeCr_2O_4$ passive film does not explain the reduction in the ORR limiting current density's dependency on rotation rate, which is illustrated in Figure 10a that shows the reverse polarization curves for Fe50Cr50 (the best ORR catalyst) in oxygenated 0.1 M NaOH at various rotation rates. It can be seen that although the limiting ORR current density increases with increasing rotation rate up to 2000 rpm, a further increase to 2500 rpm only results in minor increase in the limiting current density. The Koutecky-Levich analysis (Figure 10b) also confirms the deviation of the linear fitting at higher rotation rates.

To demonstrate that $FeCr_2O_4$ can be a good catalyst for the ORR, DFT modelling was performed to examine the ORR activity on its surface. We adopt the OH-terminated (001) surface of $FeCr_2O_4$ as the surface model shown in Figure 11, with the assumption that the exposed oxygen atoms would be hydroxylated. The approach has been used in our previous work for the chromia and hematite surfaces [22]. In addition, we choose to study the 4-electron ORR pathway (Figure 11b,11d) because it is the preferential ORR pathway for the Fe-Cr alloys as indicated by the Koutecký–Levich analysis. Figure 11b shows the free energy diagrams of the ORR on the OH-terminated $FeCr_2O_4$. The free energy evolution of the chemical species OO, OOH, O and OH on the passive layers are compared. It is found that the overall change of free energy is smaller as compared to Fe_2O_3 and Cr_2O_3 [22] and the formation of *OO, *O are exothermic, while the formation of *OH surface exhibits a flat energy barrier. The potential-determining step is the last step which forms the second H_2O. The calculated ORR overpotential for $FeCr_2O_4$ is 0.74 eV**,**

which indicates a more favourable ORR on $FeCr_2O_4$ than that on Fe_2O_3 (1.48 eV) and Cr_2O_3 (2.78 eV). The result is in good qualitative agreement with our experimental ORR overpotentials.

Another possible component of the passive films on the Fe rich alloys is Fe_3O_4 [49-51], which has the same inverse spinel structure as $FeCr_2O_4$. However, DFT calculations found that the OOH intermediate would be dissociated on an OH-terminated Fe_3O_4 surface, showing the OOH intermediate is unstable on the surface. As such, the 4-electron dissociative ORR pathway is assumed for this surface. (Figure 11d) [52]. Based on the dissociative pathway, the calculated ORR overpotential for Fe_3O_4 is 2.29 eV**,** which still indicates a more favourable ORR than on Cr_2O_3 but not as favourable as on Fe_2O_3. Nevertheless, the order of the calculated ORR overpotentials Cr_2O_3 > Fe_3O_4 > Fe_2O_3 > $FeCr_2O_4$ (2.78 eV >2.29 eV >1.48 eV >0.74 eV) remains consistent with our experimentally determined ORR onset potentials regardless as to one considers the excess iron to exist as Fe_3O_4 or Fe_2O_3. Finally, it should be noted that the efficiency of ORR on a passive film as determined in an electrochemical experiment will not only be a function of the overpotential calculated from DFT, but also of the conductivity (electronic or ionic) of the passive film as this controls the migration of the charge to the substrate. The fact that Fe_3O_4 is a far better electronic conductor than the other three oxides considered ($FeCr_2O_4$ is predicted to be an insulator [53]) may result in a better relative ORR performance on Fe_3O_4 than expected from its DFT calculated overpotential. Unfortunately, there are no existing computational methods that can take passive film conductivities into account when predicting electrochemical reaction efficiencies, largely due to the limited number of atoms present computers can handle in DFT calculations.

Potentiodynamic polarization curves in 3.5 wt.% NaCl revealed no passive region for pure iron, pitting for the Fe85Cr15 and Fe75Cr25 alloys and transpassive behaviour (no pitting) for the higher Cr content alloys (Figure S2). Weight loss tests in ferric chloride, along with photographic images collected at the end of the tests, also confirmed the increasing pitting resistance with increasing Cr content (Figures S4 & S5, Table S5). These results were as expected, as it is well known that stainless steels with higher Cr content have better resistance to pitting corrosion [54]. Nevertheless, it does show that despite the DFT calculations are in excellent agreement with the relative catalytic abilities of $FeCr_2O_4 > Fe_2O_3 > Cr_2O_3$, the fact that the passive film on Fe50Cr50 is a good ORR catalyst appears to contradict the original postulation that pitting resistance should correlate to a lower ORR rate.

However, referring back to the calculated Pourbaix diagrams in Figure 9 and Figure S6, one can observe that for solutions above about pH 5.5 the thermodynamically favourable composition of the passive film changes as the potential is increased, with the $FeCr_2O_4$ component being oxidized to form a mixture of Fe_2O_3 and Cr_2O_3. Furthermore, the line demarcating this transition is independent of the alloy's Cr content and has the same slope as (and thus parallel to) the reversible hydrogen line. As a result, when expressed against RHE the transition from $FeCr_2O_4$ to a mixture of Fe_2O_3 and Cr_2O_3 occurs at the same potential, about 0.55 V vs RHE, regardless of the pH of the environment. Armed with this knowledge, one realizes that pitting only occurs at the positive potentials above the $FeCr_2O_4$ to $Fe_2O_3 + Cr_2O_3$ transitions line, even for the least resistant Fe85Cr15 the pitting potential was ca. 0.768 V vs RHE. Indeed, even regular metastable pitting was not observed until ca. 0.600 V vs RHE (there was one small event at 0.415 V vs RHE, but this may have been noise rather than a metastable pit) (Figure S2).

Nonetheless, one needs to recognize that pitting information obtained from potential control experiments is not related to the kinetics of the cathodic reaction, as this is occurring on the counter electrode. Nevertheless, the pitting and metastable potentials deter- mined from potentiodynamic experiments should, at least in theory, be comparable to the potential at which pitting initiates under open- circuit conditions. To test this hypothesis, the Fe85Cr15 and Fe75Cr25 alloys where subjected to long-term OCP tests in 3.5 wt % NaCl at pH 6.3. Figure 12 shows the OCP of these two alloys over a period of 430 h that shows steady ennoblement of the OCP took place, which is commonly observed when stainless steels are exposed to seawater over long time periods. For example, for OCP of the Fe85Cr15 alloy increased from −0.224 V to 0.019 V vs SCE (0.390 V to 0.633 V vs RHE) meaning that after 18 days the OCP was between the metastable and critical pitting potentials determined from the potentiodynamic experiments for this alloy which were 0.600 V and 0.768 V vs RHE respectively (Fig. S2); note that the OCP of a Pt wire in the same solution was 0.190 V vs SCE (0.805 V vs RHE) at this point in time.

Only one single metastable pitting event (negative potential transit) was observed in the long-term OCP tests, which was on the Fe85Cr15 alloy after 326 h and occurred at an OCP of 0.013 V vs SCE (0.628 V vs SCE), which is in good agreement with the onset of metastable pitting observed in the potentiodynamic polarization tests (Fig. S2). The reason only a single metastable pitting event was observed may have been because OCP measurements were only recorded every 5 min, whereas metastable pits are only expected to have lifetimes of a few seconds. Nevertheless, no additional metastable pitting events were observed after the recording fre- quency was reduced to 1 s for a period of 24 h. However, Pistorius and Burstein have previously shown that the frequency of metastable pitting events decreases with time, due to the elimination of pit nucleation sites from the surface of the electrode, so after nearly 18 days such events may

be rare. Furthermore, Fig. 12 shows that although the OCP of the Fe75Cr25 alloy is initially more positive than that of its Fe85Cr15 counterpart, within a few h this trend is reversed and the Fe75Cr25 has the more the more negative OCP of the two alloys for the remainder of the 430 h experiment. This is consistent with the notion that a reduction in the ORR kinetics, due to a higher Cr_2O_3 content in the passive film, retards the ennoblement process. A retarded rate of ennoblement would delay, or could even in certain environments prevent, the onset of pitting, as this should only occur once the OCP shifts positive of the critical pitting potential. Importantly, after 430 h the OCPs of both the Fe85Cr15 and Fe75Cr25 alloys were positive of the potential (0.55 vs RHE) that the Pourbaix diagram (Fig. 9) predicts oxidation of $FeCr_2O_4$ to a mixture of Fe_2O_3 and Cr_2O_3. Therefore, when pitting, or even metastable pitting, occurs the passive film is expected to be comprised of Fe_2O_3 and Cr_2O_3, not the ORR catalytic $FeCr_2O_4$. Hence, the original premise that one role the Cr additions play in the prevention of pitting is to suppress the ORR reaction still holds. To induce pitting corrosion on the Fe85Cr15 alloys, hydrogen peroxide was added to the NaCl solution to raise the OCP (the authors are aware that the ORR would no longer be the dominate cathodic reaction). Pitting eventually occurred at approx. 0.475 V vs SCE (1.085 V vs RHE), about 300 mV more positive than the pitting potential determined from the potentiodynamic tests. A more positive pitting potential was expected from the long-term OCP tests, as Pistorius and Burstein reported the elimination of pit nucleation sites over time (i.e. these sits are lost as metastable pits), but an increase of 300 mV is more than anticipated and warrants further investigation. Note that the OCP of a Pt wire in the same solution was 0.359 V vs SCE (0.974 V vs RHE) at the time stable pitting occurred on the Fe85Cr15 alloy.

Furthermore, RDE experiments conducted in 3.5 wt.% NaCl for pure chromium and the

Fe50Cr50 alloy confirmed the poor ORR kinetics on Cr_2O_3, even worse than in NaOH (Figure 13). For the Fe50Cr50 alloy both the ORR onset potential and the limiting current density were more negative in NaCl than in NaOH, which suggest a higher fraction of Cr_2O_3 (less $FeCr_2O_4$) in the passive film. This is consistent with reports that Cr enrichment in the passive film increases as the pH decreases [47].

Finally, one possible explanation for the reduced dependency of ORR limiting current density on the rotation rate seen in the reverse scan for the high Cr containing alloys (Figure 10), is that the high surface oxygen concentration provided by the high rotation rates inhibits the transition from a mixture of Fe_2O_3 and Cr_2O_3 to $FeCr_2O_4$, such that a high fraction of chromia remains in the passive film in the potential region where the ORR limiting current density is measured. Unfortunately, attempts to use Raman spectroscopy to verify that the extent of the transition between $FeCr_2O_4$ and a mixture of Fe_2O_3 and Cr_2O_3 could indeed occur during a potentiodynamic scan was unsuccessful, due to poor signal to noise ratio (resulting from the extreme thinness of the passive film) and the small differences between the locations of the Raman peaks of the three oxides involved.

4 Conclusions

A combination of first-principles simulations and experiments have been conducted on a range of FeCr alloys, which demonstrate that ORR kinetics on the passive film can be correlated to an alloy's resistance to pitting corrosion. The main findings are:

1) First principle DFT calculations suggest that: the overpotentials for the ORR on FeCr oxides are in the order Cr_2O_3 > Fe_3O_4 > Fe_2O_3 > $FeCr_2O_4$ (2.78 eV >2.29 eV >1.48 eV >0.74 eV), the presence of larger fractions of Cr_2O_3 within the passive film will greatly suppress the ORR kinetics,

   Both these findings were confirmed by RDE experiments in both 0.1 M NaOH and 3.5 wt% NaCl.

2) Koutecký-Levich analysis demonstrated that ORR follows a 4- electron pathway on all surfaces investigated. In contrast, analysis of the limiting current densities erroneously suggests 2-electron pathway on high Cr alloys. This is thought to be because the passive film consists of a mixture of Cr_2O_3 (poor ORR catalyst) and $FeCr_2O_4$ (good catalyst) with only the $FeCr_2O_4$ regions contributing to the measured ORR limiting current density.

3) The critical pitting potential determined for the $Fe_{85}Cr_{15}$ alloy in long-term OCP transient experiments was approximately 300 mV more positive than the value found with potentiody- namic polarization tests, likely due to the elimination of pit nucleation sites over time. However, the two techniques were in better agreement for the value of the onset potential for metastable pitting.

4) Pourbaix diagrams calculated using the Materials Project for the range of FeCr investigated, suggest that at potentials where pitting corrosion initiates the passive films should consist of a mixture of Fe_2O_3 and Cr_2O_3, rather than the catalytic $FeCr_2O_4$. This is generally in

agreement with the XPS findings in the published literature.

ACKNOWLEDGMENTS

This work was supported by the Structural Metal Alloys Programme of Agency for Science, Technology and Research (A*STAR) (A18B1b0061). The authors would like to acknowledge National University of Singapore for the facilities for the characterization and the electrochemical tests; National Supercomputing Centre (NSCC) Singapore and the A*STAR Computational Resource Centre (A*CRC) of Singapore for the use of their high-performance computing facilities.

References

[1] B. Zhang, J. Wang, B. Wu, X. W. Guo, Y. J. Wang, D. Chen, Y. C. Zhang, K. Du, E. E. Oguzie, X. L. Ma, Unmasking chloride attack on the passive film of metals, Nat. Commun. 9 (2018) 2559. https://doi.org/10.1038/s41467-018-04942-x.

[2] X. Yin, H. Wang, E.-H. Han, Cl-induced passivity breakdown in α-Fe_2O_3 (0001), α-Cr_2O_3 (0001), and their interface: A DFT study, J. Mater. Sci. Technol. 129 (2022) 70-78. https://doi.org/10.1016/j.jmst.2022.03.034.

[3] J. E. Castle, R. Ke, Studies by auger spectroscopy of pit initiation at the site of inclusions in stainless steel, Corros. Sci. 30 (1990) 409-428. https://doi.org/10.1016/0010-938X(90)90047-9.

[4] J. Stewart, D. E. Williams, The initiation of pitting corrosion on austenitic stainless steel: on the role and importance of sulphide inclusions, Corros. Sci. 33 (1992) 457-463, 465-474. https://doi.org/10.1016/0010-938X(92)90074-D .

[5] M. A. Baker, J. E. Castle, The initiation of pitting corrosion at MnS inclusions, Corros. Sci. 34 (1993) 667-682. https://doi.org/10.1016/0010-938X(93)90279-P.

[6] G. S. Frankel, Pitting corrosion of metals: A review of the critical factors, J. Electrochem. Soc. 145 (1998) 2186-2198. https://doi.org/10.1149/1.1838615.

[7] M. P. Ryan, D. E. Williams, R. J. Chater, B. M. Hutton, D. S. McPhail, Why stainless steel corrodes. Nature 415 (2002) 770-774. https://doi.org/10.1038/415770a.

[8] Q. Meng, G. S. Frankel, H. O. Colijn, S. H. Goss, Stainless-steel corrosion and MnS inclusions, Nature 424 (2003) 389-390. https://doi.org/10.1038/424389b.

[9] J. Horvath, H. H. Uhlig, Critical potentials for pitting corrosion of Ni, Cr-Ni, Cr-Fe, and related stainless steels, J. Electrochem. Soc. 115 (1968) 791-795. https://doi.org/10.1149/1.2411433.

[10] G. T. Burstein, P. C. Pistorius, S. P. Mattin, The nucleation and growth of corrosion pits on stainless steel, Corros. Sci. 35 (1993) 57-62. https://doi.org/10.1016/0010-938X(93)90133-2.

[11] J. Soltis, Passivity breakdown, pit initiation and propagation of pits in metallic materials – Review, Corros. Sci. 90 (2015) 5-22. https://doi.org/10.1016/j.corsci.2014.10.006.

[12] N.Le Bozec, C.Compère, M. L'Her, A. Laouenan, D. Costa, P. Marcus, Influence of stainless steel surface treatment on the oxygen reduction reaction in seawater, Corros. Sci. 43 (2001) 765-786. https://doi.org/10.1016/S0010-938X(00)00113-X.

[13] S. V. Phadnis, A. K. Satpati, K. P. Muthe, J. C. Vyas, R. I. Sundaresan, Comparison of rolled and heat treated SS304 in chloride solution using electrochemical and XPS techniques. Corros.

Sci. 45 (2003) 2467-2483. https://doi.org/10.1016/S0010-938X(03)00099-4.

[14] W. P. Yang, D. Costa, P. Marcus, Resistance to pitting and chemical composition of passive films of a Fe-17%Cr alloy in chloride-containing acid solution, J. Electrochem. Soc. 141 (1994) 2669-2676. https://doi.org/10.1149/1.2059166.

[15] C. Örnek, C. Leygraf, J. Pan, Passive film characterisation of duplex stainless steel using scanning Kelvin probe force microscopy in combination with electrochemical measurements. npj Mater. Degrad. 3 (2019) 8. https://doi.org/10.1038/s41529-019-0071-8.

[16] C. L. McBee, J. Kruger, Nature of passive films on iron-chromium, Electrochim. Acta 17 (1972) 1337-1341. https://doi.org/10.1016/0013-4686(72)80079-3.

[17] E. R. Vago, E. J. Calvo, Electrocatalysis of oxygen reduction at Fe_3O_4 oxide electrodes in alkaline solutions, J. Electroanal. Chem. 339 (1992) 41-67. https://doi.org/10.1016/0022-0728(92)80444-9.

[18] R. Babić, M. Metikoš-Huković, Oxygen reduction on stainless steel, J. Appl. Electrochem. 23 (1993) 352-357. https://doi.org/10.1007/BF00296691.

[19] H. S. Wroblowa, S. B. Qaderi, Mechanism and kinetics of oxygen reduction on steel, J. Electroanal. Chem. 279 (1990) 231-242. https://doi.org/10.1016/0022-0728(90)85179-9.

[20] C. L. Alexander, C. Liu, A. Alshanoon, R. M. Katona, R. G. Kelly, J. Carpenter, C. Bryan, E. Schindelholz, Oxygen reduction on stainless steel in concentrated chloride media, J. Electrochem. Soc. 165 (2018) C869-C877. https://doi.org/10.1149/2.0181813jes.

[21] C. Liu, R, G. Kelly, Comparison study of the effect of oxide film properties on cathodic kinetics of stainless steel 304L and 316L during ORR potential window in sulfate solution, Corrosion 75 (2019) 1087-1099. https://doi.org/10.5006/3134.

[22] M.-F. Ng, D. J. Blackwood, H. Jin, T. L. Tan, DFT study of oxygen reduction reaction on chromia and hematite: insights into corrosion inhibition, J. Phys. Chem. C 124 (2020) 13799-13808. https://doi.org/10.1021/acs.jpcc.0c03559.

[23] ASTM Standard G48-11(2020)e1, Standard test methods for pitting and crevice corrosion resistance of stainless steels and related alloys by use of ferric chloride solution. https://doi.org/10.1520/G0048-11R20E01.

[24] L. Meites, Handbook of analytical chemistry, first ed., McGraw Hill, New York, 1963, section 5.

[25] S. Gupta, S. Zhao, X. X. Wang, S. Hwang, S. Karakalos, S. V. Devaguptapu, S. Mukherjee, D. Su, H. Xu, G. Wu, Quaternary FeCoNiMn-based nanocarbon electrocatalysts for bifunctional

oxygen reduction and evolution: promotional role of Mn doping in stabilizing carbon, ACS Catal. 7 (2017) 8386-8393. https://doi.org/10.1021/acscatal.7b02949.

[26] H. Zhao, C. Sun, Z. Jin, D.-W. Wang, X. Yan, Z. Chen, G. Zhu, X. Yao, Carbon for the oxygen reduction reaction: a defect mechanism, J. Mater. Chem. A, 2015,3, 11736-11739. https://doi.org/10.1039/C5TA02229K.

[27] J. P. Perdew, K. Burke, M. Ernzerhof, Generalized gradient approximation made simple, Phys. Rev. Lett. 77 (1996) 3856-3868. https://doi.org/10.1103/PhysRevLett.77.3865.

[28] G. Kresse, J. Furthmuller, Efficient iterative schemes for ab initio total-energy calculations using a plane-wave basis set, Phys. Rev. B 54 (1996) 11169-11186. https://doi.org/10.1103/PhysRevB.54.11169.

[29] P. E. Blöchl, Projector augmented-wave method, Phys. Rev. B 50 (1994) 17953-17979. https://doi.org/10.1103/PhysRevB.50.17953.

[30] V. I. Anisimov, J. Zaanen, O. K. Andersen, Band theory and Mott insulators: Hubbard U instead of Stoner I, Phys. Rev. B 44 (1991) 943-954. https://doi.org/10.1103/PhysRevB.44.943.

[31] S. L. Dudarev, G. A. Botton, S. Y. Savrasov, C. J. Humphreys, A. P. Sutton, Electron-energy-loss spectra and the structural stability of nickel oxide: an LSDA+U Study, Phys. Rev. B 57 (1998) 1505-1509. https://doi.org/10.1103/PhysRevB.57.1505.

[32] K. Jiang, S. Back, A. J. Akey, C. Xia, Y. Hu, W. Liang, D. Schaak, E. Stavitski, J. K. Nørskov, S. Siahrostami, H. Wang, Highly selective oxygen reduction to hydrogen peroxide on transition metal single atom coordination, Nat. Comm. 10 (2019) 3997. https://doi.org/10.1038/s41467-019-11992-2.

[33] A. Jain, S. P. Ong, G. Hautier, W. Chen, W. D. Richards, S. Dacek, S. Cholia, D. Gunter, D. Skinner, G. Ceder, K. A. Persson, Commentary: the materials project: a materials genome approach to accelerating materials innovation, APL Mater. 1 (2013) 011002. https://doi.org/10.1063/1.4812323.

[34] K. A. Persson, B. Waldwick, P. Lazic, G. Ceder, Prediction of solid-aqueous equilibria: scheme to combine first-principles calculations of solids with experimental aqueous states, Phys. Rev. B 85 (2012) 235438. https://doi.org/10.1103/PhysRevB.85.235438.

[35] A. K. Singh, L. Zhou, A. Shinde, S. K. Suram, J. H. Montoya, D. Winston, J. M. Gregoire, K. A. Persson, Electrochemical stability of metastable materials, Chem. Mater. 29 (2017) 10159-10167. https://doi.org/10.1021/acs.chemmater.7b03980.

[36] V. Jovancicevic, J. O'M. Bockris, The mechanism of oxygen reduction on iron in neutral solutions, J. Electrochem. Soc. 133 (1986) 1797-1807. https://doi.org/10.1149/1.2109021.

[37] E.J. Calvo, D.J. Schifrin, The reduction of hydrogen peroxide on passive iron in alkaline solutions, J. Electroanal. Chem. 163 (1984) 257-275. https://doi.org/10.1016/S0022-0728(84)80056-X.

[38] E. Samson, J. Marchand, K. A. Snyder, Calculation of ionic diffusion coefficients on the basis of migration test results, Mat. Struct. 36 (2003) 156-165. https://doi.org/10.1007/BF02479554.

[39] B. B. Blizanac, P. N. Ross, N. M. Marković, Oxygen reduction on silver low-index single-crystal surfaces in alkaline solution: rotating ring disk$_{Ag(hkl)}$ studies, J. Phys. Chem. B 110 (2006) 4735-4741. https://doi.org/10.1021/jp056050d.

[40] C. A. Campos-Roldán, R. G. González-Huerta, N. Alonso-Vante, Experimental protocol for HOR and ORR in alkaline electrochemical measurements, J. Electrochem. Soc, 165 (2018) J3001-J3007. https://doi.org/10.1149/2.0011815jes.

[41] K. Nagata, R. Nishiwaki, Y. Nakamura, T. Maruyama, Kinetic mechanisms of the formations of $MgCr_2O_4$ and $FeCr_2O_4$ spinels from their metal oxides, Solid State lon. 49 (1991) 161-166. https://doi.org/10.1016/0167-2738(91)90081-L.

[42] T. L. Sudesh, L. Wijesinghe, D. J. Blackwood, Characterisation of passive films on 300 series stainless steels, Appl. Surf. Sci. 253 (2006) 1006-1009. https://doi.org/10.1016/j.apsusc.2006.03.081.

[43] M. B. Shafqat, M. Ali, S. Atiq, S. M. Ramay, H. M. Shaikh, S. Naseem, Structural, morphological and dielectric investigation of spinel chromite (XCr_2O_4, X = Zn, Mn, Cu & Fe) nanoparticles, J. Mater. Sci.: Mater. Electron. 30 (2019) 17623–17629. https://doi.org/10.1007/s10854-019-02111-4.

[44] V. D'Ippolito, G. B. Andreozzi, D. Bersani, P. P. Lottici, Raman fingerprint of chromate, aluminate and ferrite spinels, J. Raman Spectrosc. 46 (2015) 1255-1264. https://doi.org/10.1002/jrs.4764.

[45] A. Boudjemaa, R. Bouarab, S. Saadi, A. Bouguelia, M. Trari, Photoelectrochemical H_2-generation over Spinel $FeCr_2O_4$ in X^{2-} solutions (X^{2-}= S^{2-} and SO_3^{2-}), Appl. Energ. 86 (2009) 1080–1086. https://doi.org/10.1016/j.apenergy.2008.06.007.

[46] C. Calinski, H.-H. Strehblow, ISS depth profiles of the passive layer on Fe/Cr alloys, J. Electrochem. Soc. 136 (1989) 1328-1331. https://doi.org/10.1149/1.2096915.

[47] C.-O. A. Olsson, D. Landolt, Passive films on stainless steels - chemistry, structure and growth, Electrochim. Acta, 48 (2003) 1093-1104. https://doi.org/10.1016/S0013-4686(02)00841-1.

[48] H.-H. Strehblow, Passivity of metals studied by surface analytical methods, a review, Electrochim. Acta 212 (2016) 630-648. https://doi.org/10.1016/j.electacta.2016.06.170.

[49] M. Stratmann, J. Müller, The mechanism of the oxygen reduction on rust-covered metal substrates, Corros. Sci. 36 (1994) 327-359. https://doi.org/10.1016/0010-938X(94)90161-9.

[50] S. Lj. Gojkovic, S. K. Zecevic, D. M. Drazic, Oxygen reduction on iron—part VI. processes in alkaline solutions, Electrochim. Acta 39 (1994) 975-982. https://doi.org/10.1016/0013-4686(94)85115-8.

[51] E. Zaki, F. Mirabella, F. Ivars-Barceló, J. Seifert, S. Carey, S. Shaikhutdinov, H.-J. Freund, X. Li, J. Paier, J. Sauer, Water adsorption on the Fe_3O_4(111) surface: dissociation and network formation, Phys. Chem. Chem. Phys. 20 (2018) 15764-15774. https://doi.org/10.1039/c8cp02333f.

[52] J. K. Nørskov, J. Rossmeisl, A. Logadottir, L. Lindqvist, J. R. Kitchin, T. Bligaard, H. Jónsson, Origin of the overpotential for oxygen reduction at a fuel-cell cathode, J. Phys. Chem. B 108 (2004) 17886-17892. https://doi.org/10.1021/jp047349j.

[53] S. A. Chambers, T. C. Droubay, T. C. Kaspar, I. H. Nayyar, M. E. McBriarty, S. M. Heald, D. J. Keavney, M. E. Bowden, P. V. Sushko, Electronic and optical properties of a semiconducting spinel (Fe_2CrO_4), Adv. Funct. Mater. 27 (2017) 1605040. https://doi.org/10.1002/adfm.201605040.

[54] R. F. Steigerwald, Effect of Cr content on pitting behavior of Fe-Cr alloys, Corrosion 22 (1966) 107-112. https://doi.org/10.5006/0010-9312-22.4.107.

Figure Legends

Figure 1. SEM-EDS analysis of Fe35Cr65 alloy (a) SEM image of Fe35Cr65 alloy, (b) EDS mapping of Fe distributed in the Fe35Cr65 alloy, (c) EDS mapping of Cr distributed in the Fe35Cr65 alloy, (d) Cr content of the FeCr alloys calculated based on the EDS results.

Figure 2. X-ray diffraction (XRD) patterns of the as-cast FeCr alloys.

Figure 3. Polarization curves of the oxygen reduction reactions on Fe and Cr electrodes in 0.1 M NaOH at various rotation rates: (a) Fe forward scan; (b) Fe reverse scan; (c) Cr forward scan; (d) Cr reverse scan; (e) comparison of forward and reverse scans at 1500 rpm on Fe and (f) on Cr.

Figure 4. Comparison of ORR on the surfaces of Fe and Cr electrodes in O_2 saturated 0.1 M NaOH: (a) forward scan at 1500 rpm, (b) reverse scan at 1500 rpm.

Figure 5. Koutecky-Levich plots at various electrode potentials (vs. RHE) in O_2 saturated 0.1 M NaOH. (a) Fe forward scan, (b) Fe reverse scan, (c) Cr forward scan.

Figure 6. Polarization curves of FeCr alloys at 1500 rpm in O_2 saturated 0.1 NaOH from (a) forward scans, (b) reverse scans, (c) & (d) comparisons of forward and reverse scans for alloys Fe75Cr25 and Fe25Cr75, respectively.

Figure 7. Plot of the measured limiting current densities recorded at different rotation rates (100 rpm, 1500 rpm & 2500 rpm) for the forward (solid symbols) and reverse (open symbols) scans against the alloy composition. Marked on the plot are the theoretical limiting current densities expected for an oxygen saturated solution (1.22×10^{-6} mol cm^{-3}) undergoing the 2 electron (dashed lines) and 4-electron (solid lines) pathways at the specified rotations rates.

Figure 8. Comparison of the ORR onset potentials of the FeCr alloys from reverse scans in O_2 saturated 0.1 M NaOH.

Figure 9. Pourbaix diagrams of FeCr alloys obtained using the *Materials Project* [33-35].

Figure 10. (a) Polarization curves of the oxygen reduction reaction on Fe50Cr50 at various rotation rates in 0.1 M NaOH (reverse scans), (b) Koutecky-Levich plots of Fe50Cr50 at various electrode potentials (reverse scan, V vs. RHE).

Figure 11. (a) Side views of the $FeCr_2O_4$ and Fe_3O_4 (001) surfaces. (b) The 4-electron associative ORR pathway on the (001) OH-terminated $FeCr_2O_4$ surface, and (c) the associated Gibbs free energy diagram at the equilibrium potential. (d) The 4-electron dissociative ORR pathway on the (001) OH-terminated Fe_3O_4 surface, and (d) the associated Gibbs free energy diagram at the equilibrium potential. Note that for the dissociative mechanism, only half of the reaction is shown (as two *O undergo the same pathway). The overpotentials (η) of each reaction are marked in the insets.

Figure 12. long-term OCP transients for Fe85Cr15 and Fe75Cr25 alloys in 3.5 wt% NaCl (pH = 6.3) exposed to the natural atmosphere. Note 0 V vs SCE = 0.615 V vs RHE.

Figure 13. Polarization curve of pure Cr and Fe50Cr50 in 0.1 M NaOH (pH=13) and 3.5 wt.% NaCl (pH=6.3) at 100 rpm.

Table Legends

Table 1. Summary of the fitting results for the Koutecky-Levich plots of Fe and Cr at various electrode potentials (-0.018 V, -0.068 V, and -0.118 V vs. RHE; -0.95 V, -1.0 V and -1.05 V vs. Hg/HgO (0.1M NaOH)) shown in Figure 5.

Table 2. Summary of the onset potentials/ overpotentials (1500 rpm) and the possible compositions of the passive film on FeCr alloys in 0.1 M NaOH as determined from Pourbaix diagrams calculated using the *Materials Project* [33-35].

Figures

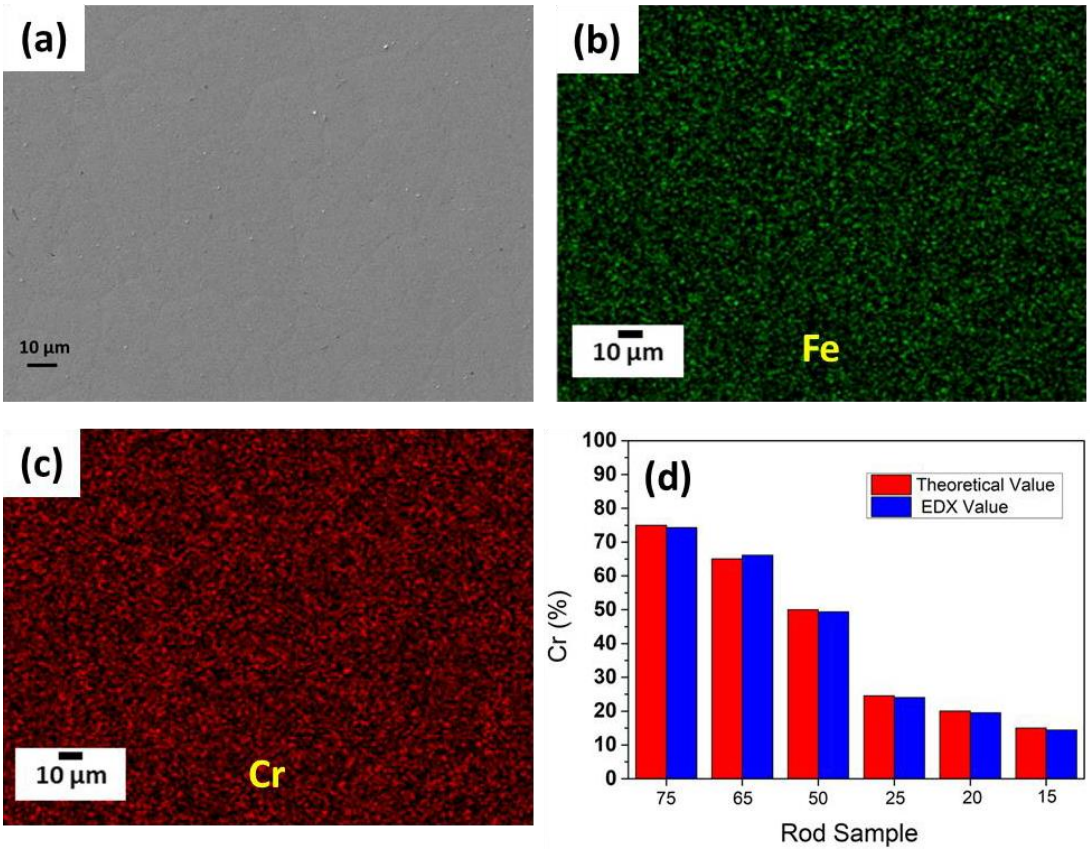

Figure 1. SEM-EDS analysis of Fe35Cr65 alloy (a) SEM image of Fe35Cr65 alloy, (b) EDS mapping of Fe distributed in the Fe35Cr65 alloy, (c) EDS mapping of Cr distributed in the Fe35Cr65 alloy, (d) Cr content of the FeCr alloys calculated based on the EDS results.

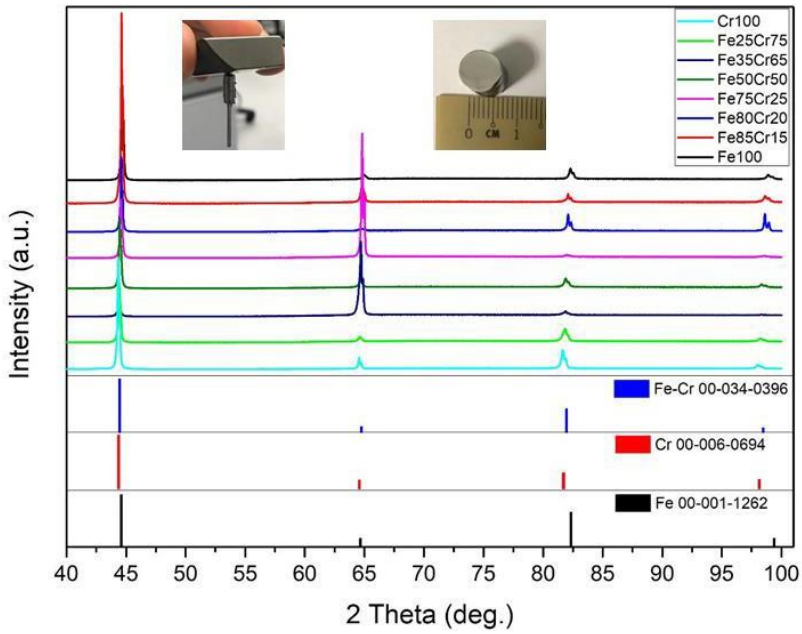

Figure 2. X-ray diffraction (XRD) patterns of the as-cast FeCr alloys.

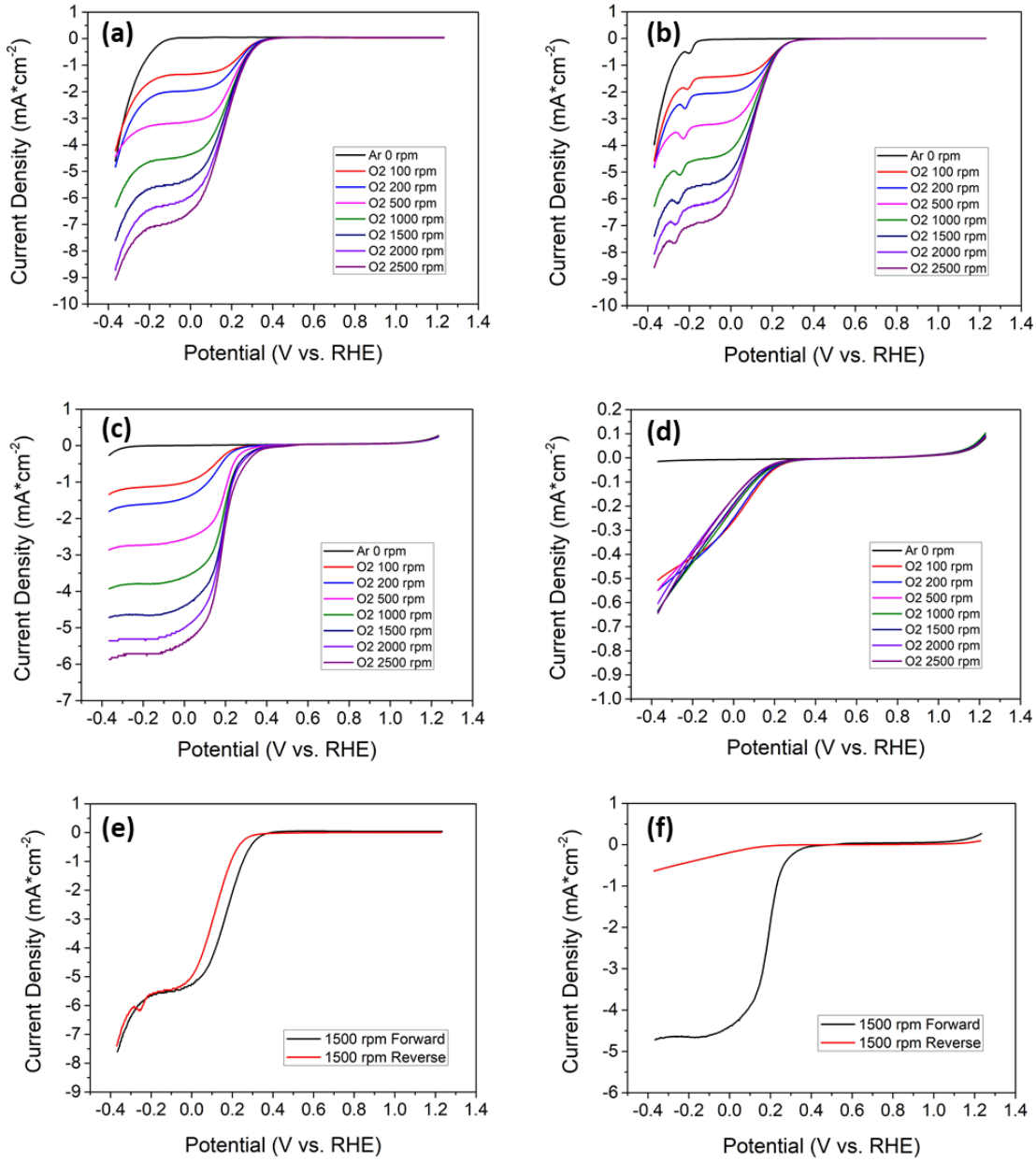

Figure 3. Polarization curves of the oxygen reduction reactions on Fe and Cr electrodes in 0.1 M NaOH at various rotation rates: (a) Fe forward scan; (b) Fe reverse scan; (c) Cr forward scan; (d) Cr reverse scan; (e) comparison of forward and reverse scans at 1500 rpm on Fe and (f) on Cr.

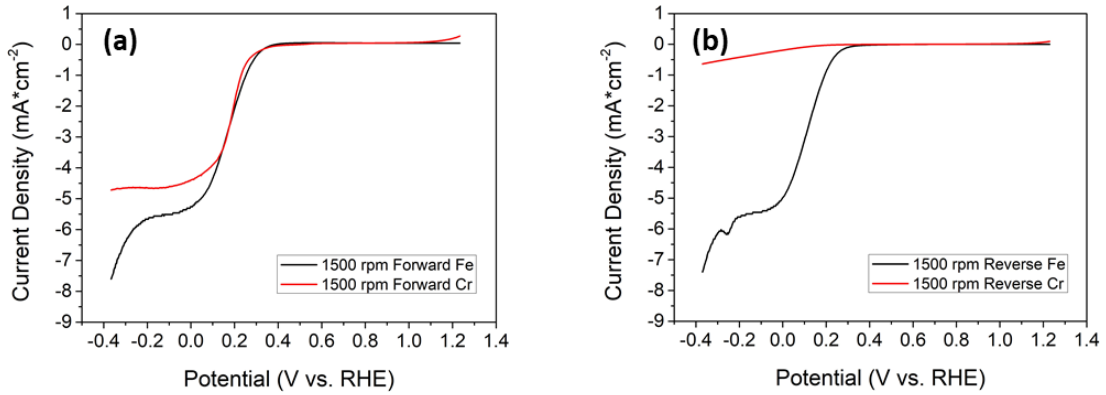

Figure 4. Comparison of ORR on the surfaces of Fe and Cr electrodes in O_2 saturated 0.1 M NaOH: (a) forward scan at 1500 rpm, (b) reverse scan at 1500 rpm.

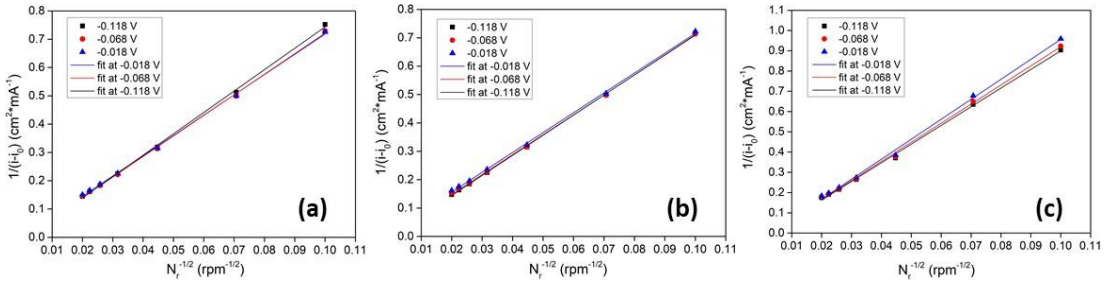

Figure 5. Koutecky-Levich plots at various electrode potentials (vs. RHE) in O_2 saturated 0.1 M NaOH. (a) Fe forward scan, (b) Fe reverse scan, (c) Cr forward scan.

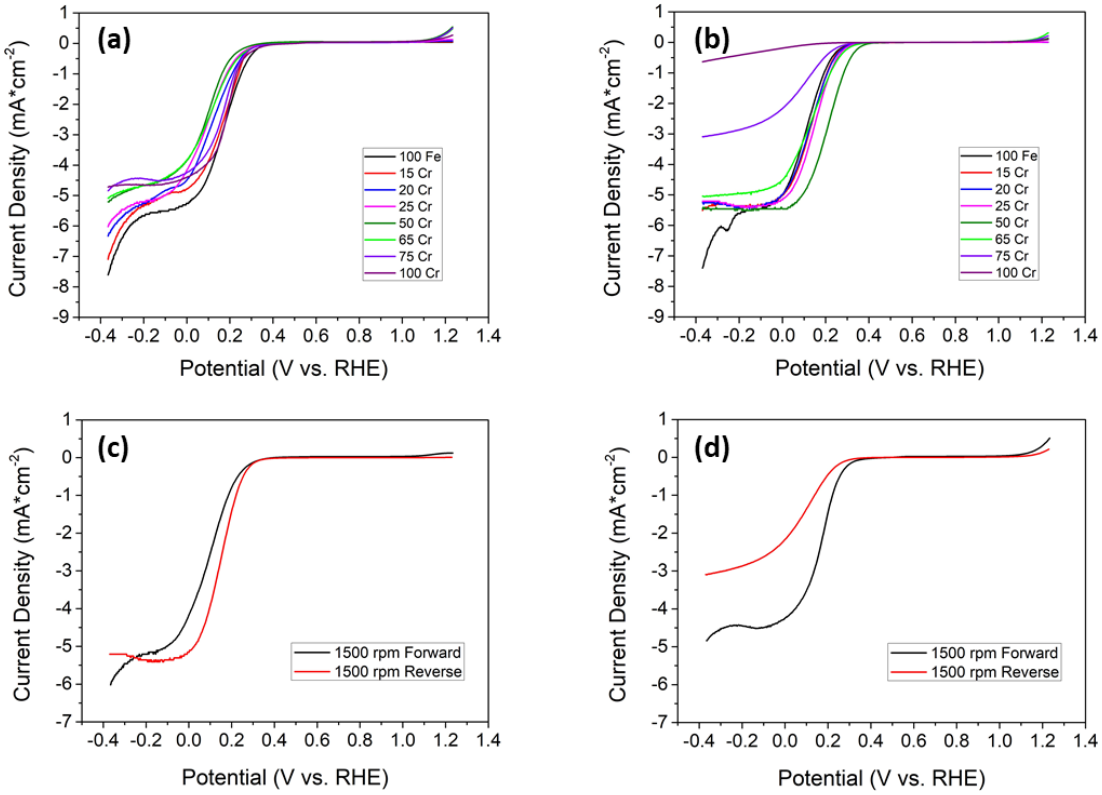

Figure 6. Polarization curves of FeCr alloys at 1500 rpm in O_2 saturated 0.1 NaOH from (a) forward scans, (b) reverse scans, (c) & (d) comparisons of forward and reverse scans for alloys Fe75Cr25 and Fe25Cr75, respectively.

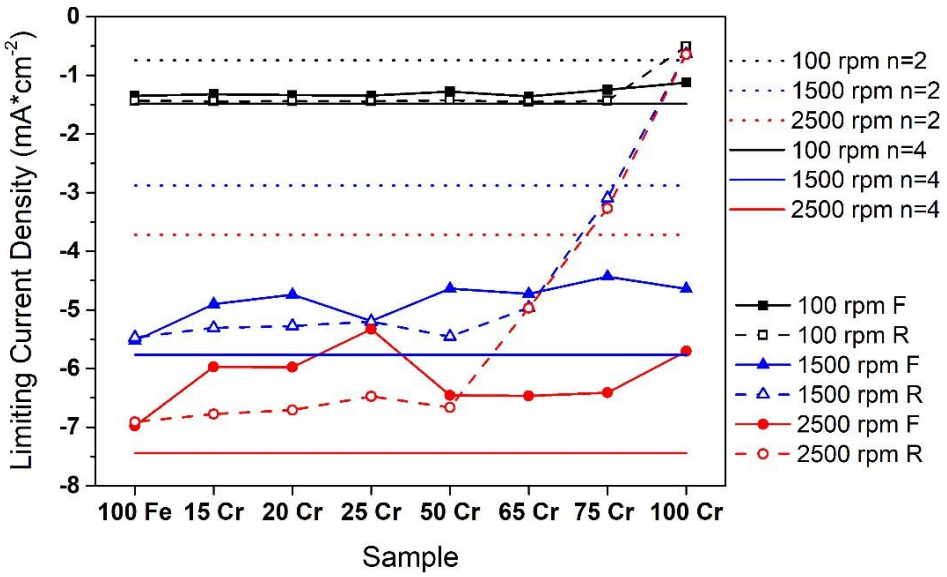

Figure 7. Plot of the measured limiting current densities recorded at different rotation rates (100 rpm, 1500 rpm & 2500 rpm) for the forward (solid symbols) and reverse (open symbols) scans against the alloy composition. Marked on the plot are the theoretical limited current densities expected for an oxygen saturated solution (1.22×10^{-6} mol cm^{-3}) undergoing the 2 electron (dashed lines) and 4-electron (solid lines) pathways at the specified rotations rates.

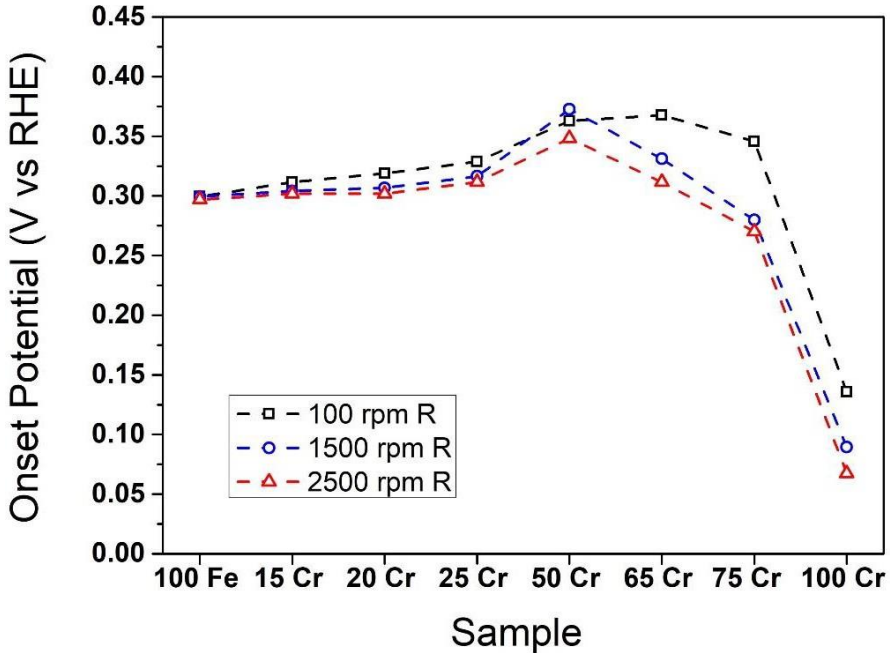

Figure 8. Comparison of the ORR onset potentials of the FeCr alloys from reverse scans in O_2 saturated 0.1 M NaOH.

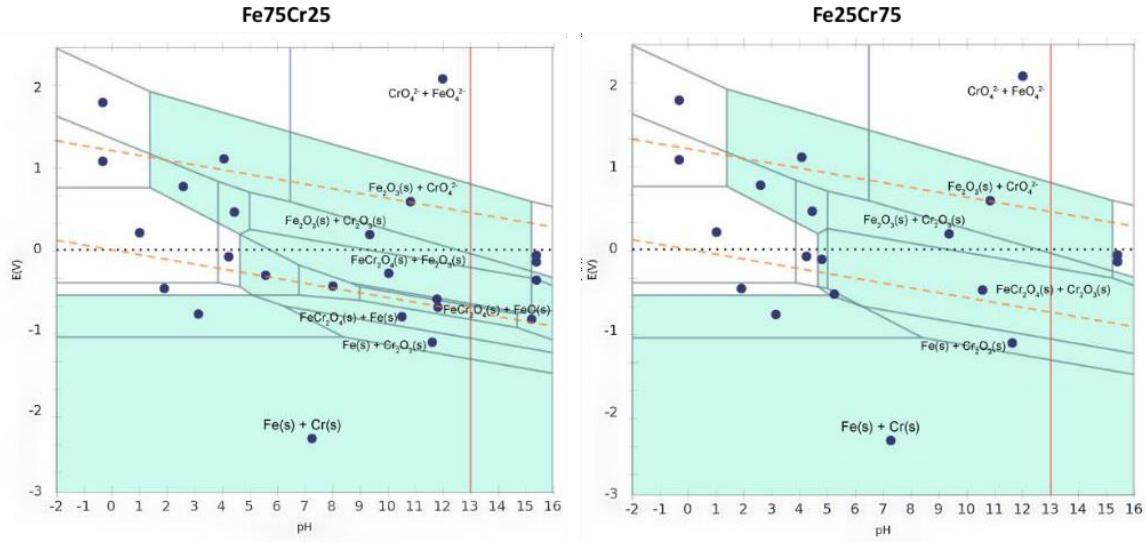

Figure 9. Pourbaix diagrams of FeCr alloys obtained using the *Materials Project* [33-35].

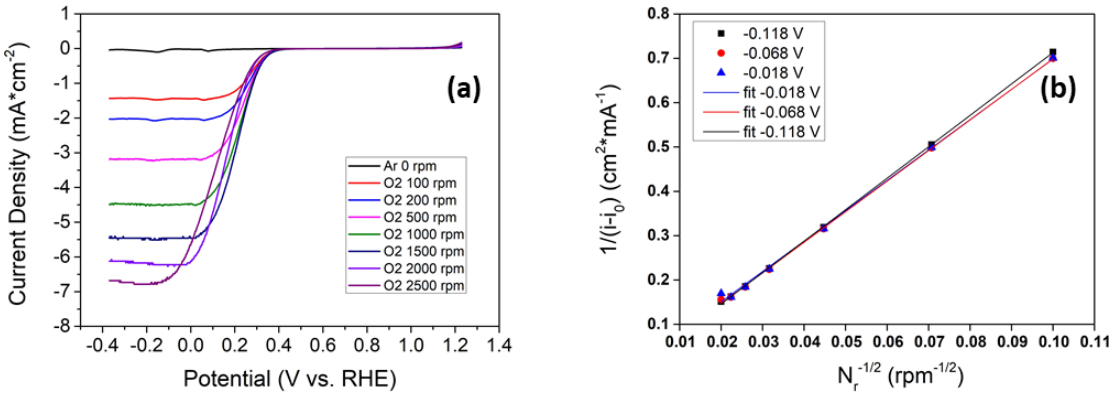

Figure 10. (a) Polarization curves of the oxygen reduction reaction on Fe50Cr50 at various rotation rates in 0.1 M NaOH (reverse scans), (b) Koutecky-Levich plots of Fe50Cr50 at various electrode potentials (reverse scan, V vs. RHE).

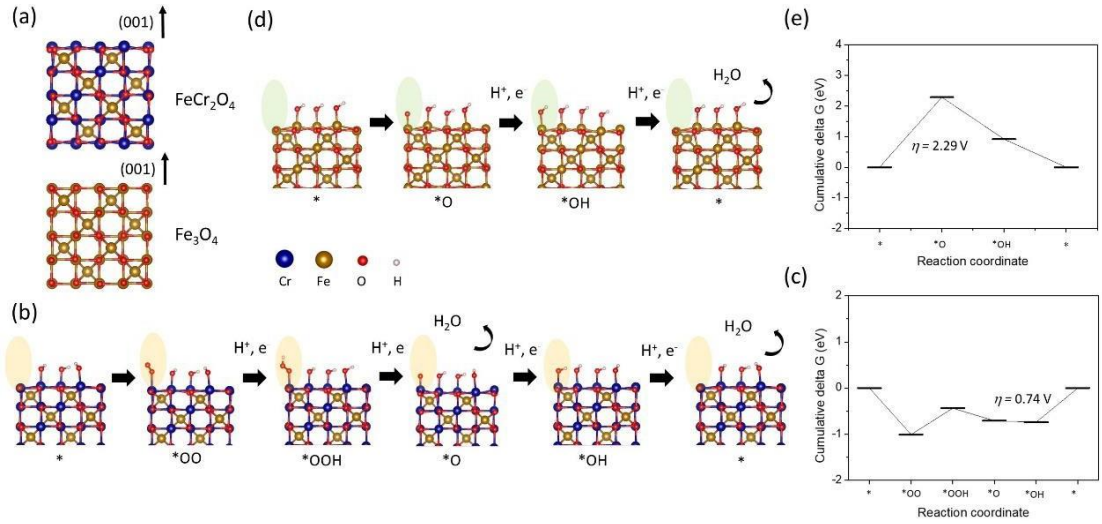

Figure 11. (a) Side views of the $FeCr_2O_4$ and Fe_3O_4 (001) surfaces. (b) The 4-electron associative ORR pathway on the (001) OH-terminated $FeCr_2O_4$ surface, and (c) the associated Gibbs free energy diagram at the equilibrium potential. (d) The 4-electron dissociative ORR pathway on the (001) OH-terminated Fe_3O_4 surface, and (d) the associated Gibbs free energy diagram at the equilibrium potential. Note that for the dissociative mechanism, only half of the reaction is shown (as two *O undergo the same pathway). The overpotentials (η) of each reaction are marked in the insets.

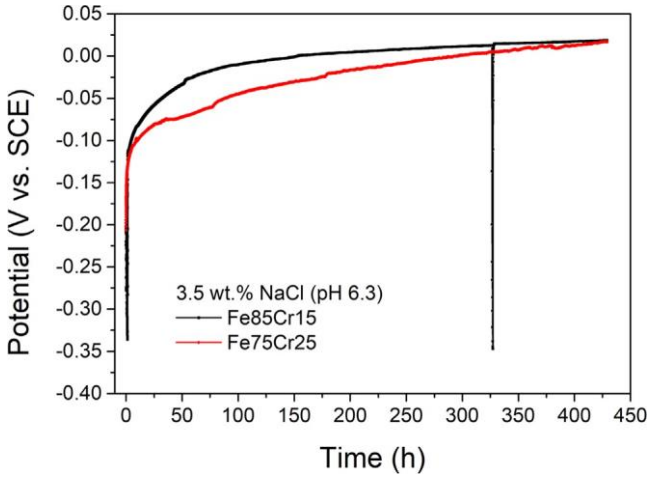

Figure 12. long-term OCP transients for Fe85Cr15 and Fe75Cr25 alloys in 3.5 wt% NaCl (pH = 6.3) exposed to the natural atmosphere. Note 0 V vs SCE = 0.615 V vs RHE.

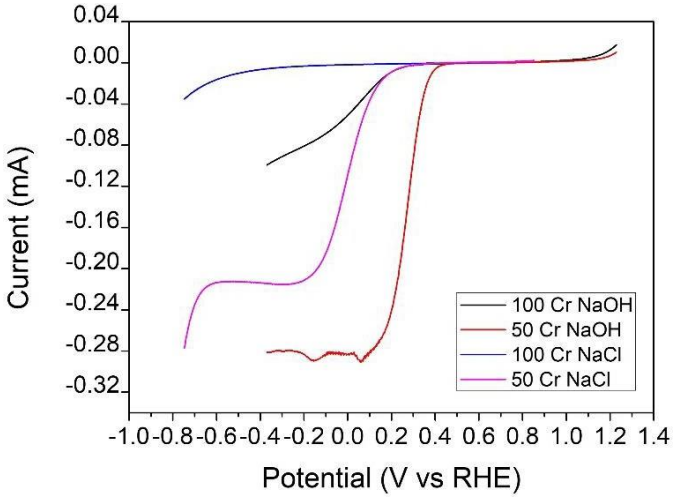

Figure 13. Polarization curve of pure Cr and Fe50Cr50 in 0.1 M NaOH (pH=13) and 3.5 wt.% NaCl (pH=6.3) at 100 rpm.

Table 1. Summary of the fitting results for the Koutecky-Levich plots of Fe and Cr at various electrode potentials (-0.018 V, -0.068 V, and -0.118 V vs. RHE; -0.95 V, -1.0 V and -1.05 V, vs. Hg/HgO (0.1M NaOH)) shown in Figure 5.

Forward Scan	**Fitting Equation**	**n**
Fe -0.118 V	y = 7.56 x - 0.0121	3.56
Fe -0.068 V	y = 7.27 x - 0.0051	3.71
Fe -0.018 V	y = 7.17 x + 0.0012	3.75
Cr -0.118 V	y = 9.21 x - 0.0210	2.92
Cr -0.068 V	y = 9.43 x - 0.0232	2.86
Cr -0.018 V	y = 9.86 x - 0.0294	2.73
Reverse Scan	**Fitting Equation**	**n**
Fe -0.118 V	y = 7.08 x + 0.0026	3.80
Fe -0.068 V	y = 7.01 x + 0.0076	3.84
Fe -0.018 V	y = 7.00 x + 0.0161	3.85

Table 2. Summary of the onset potentials/ overpotentials (1500 rpm) and the possible compositions of the passive film on FeCr alloys in 0.1 M NaOH as determined from Pourbaix diagrams calculated using the *Materials Project* [33-35].

Sample		Onset Potential/V vs. RHE	Experimental Overpotential/V	Thermodynamically stable constitution based on Pourbaix diagram	Mole fraction of $FeCr_2O_4$* in passive film
Wt%	At%				
Fe100	Fe100	0.299	0.93	Fe_3O_4/Fe_2O_3	0
Fe85Cr15	Fe85Cr15	0.304	0.93	$Fe_3O_4/Fe_2O_3 + FeCr_2O_4$	0.17
Fe80Cr20	Fe79Cr21	0.307	0.92	$Fe_3O_4/Fe_2O_3 + FeCr_2O_4$	0.23
Fe75Cr25	Fe74Cr26	0.316	0.91	$Fe_3O_4/Fe_2O_3 + FeCr_2O_4$	0.31
Fe50Cr50	Fe48Cr52	0.373	0.86	$Fe_3O_4/Fe_2O_3 + FeCr_2O_4$	0.70
Fe35Cr65	Fe33Cr67	0.331	0.90	$FeCr_2O_4$	1.00
Fe25Cr75	Fe24Cr76	0.280	0.95	$Cr_2O_3 + FeCr_2O_4$	0.63
Cr100	Cr100	0.089	1.14	Cr_2O_3	0

*Assuming remainder of passive film is either Fe_2O_3 or Cr_2O_3.

Supporting Information

Supporting Figures

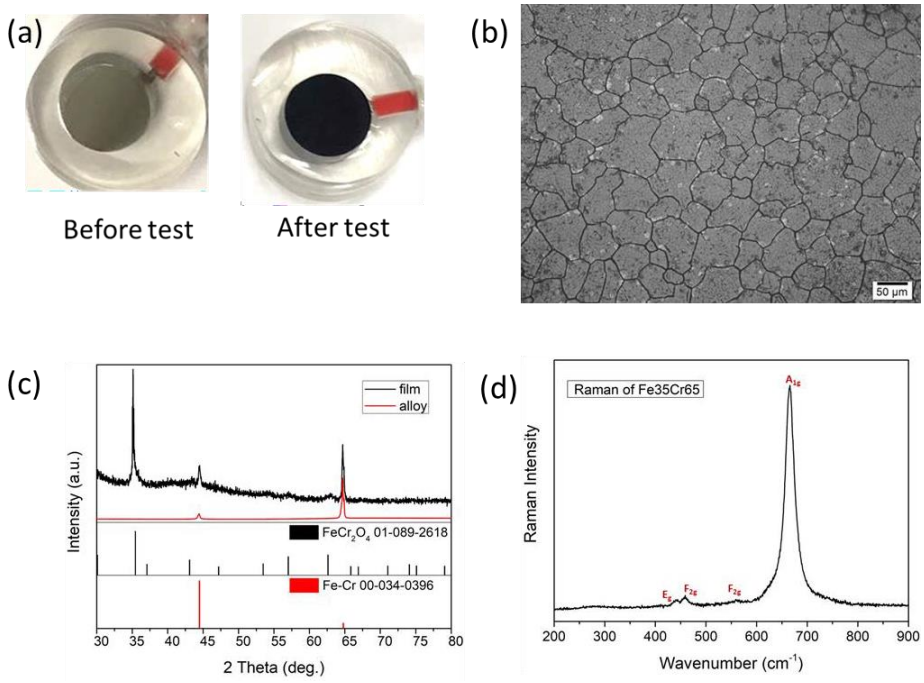

Figure S1. (a) Fe35Cr65 sample before and after being cycled voltametric scanned into the transpassive region at 0.65 V and returned to -1.3 V vs Hg/HgO (0.1 M NaOH) (b) microscopic image (c) XRD pattern (d) and Raman spectra of the surface after the cyclic voltammetry.

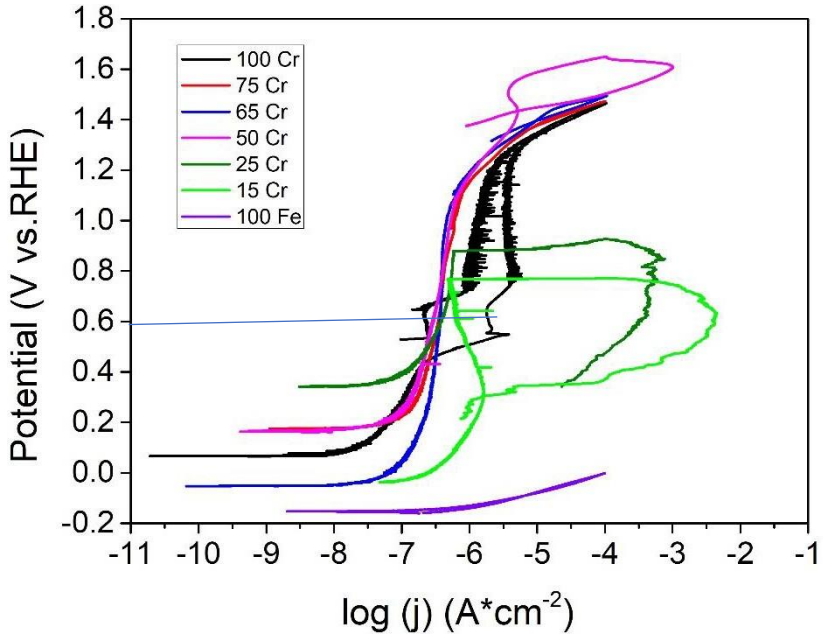

Figure S2. Potentiodynamic polarization curves of FeCr alloys at 0.1667 mV/s^{-1} in 3.5 wt.% NaCl (vs. RHE).

The 4-eletron ORR associative pathway:

$$O_2 + * \rightarrow *OO \quad (1)$$

$$*OO + H^+ + e^- \rightarrow *OOH \quad (2)$$

$$*OOH + H^+ + e^- \rightarrow H_2O + *O \quad (3)$$

$$*O + H^+ + e^- \rightarrow *OH \quad (4)$$

$$*OH + H^+ + e^- \rightarrow H_2O + * \quad (5)$$

The 4-electron ORR dissociative pathway:

$$1/2O_2 + * \rightarrow *O \quad (6)$$

$$*O + H^+ + e^- \rightarrow *OH \quad (7)$$

$$*OH + H^+ + e^- \rightarrow H_2O + * \quad (8)$$

Figure S3. The equations of the 4-electron associative and dissociative ORR mechanisms. Note that for the dissociative pathway, two *O will form from an O_2 molecule. So overall it is a 4-electron reaction.

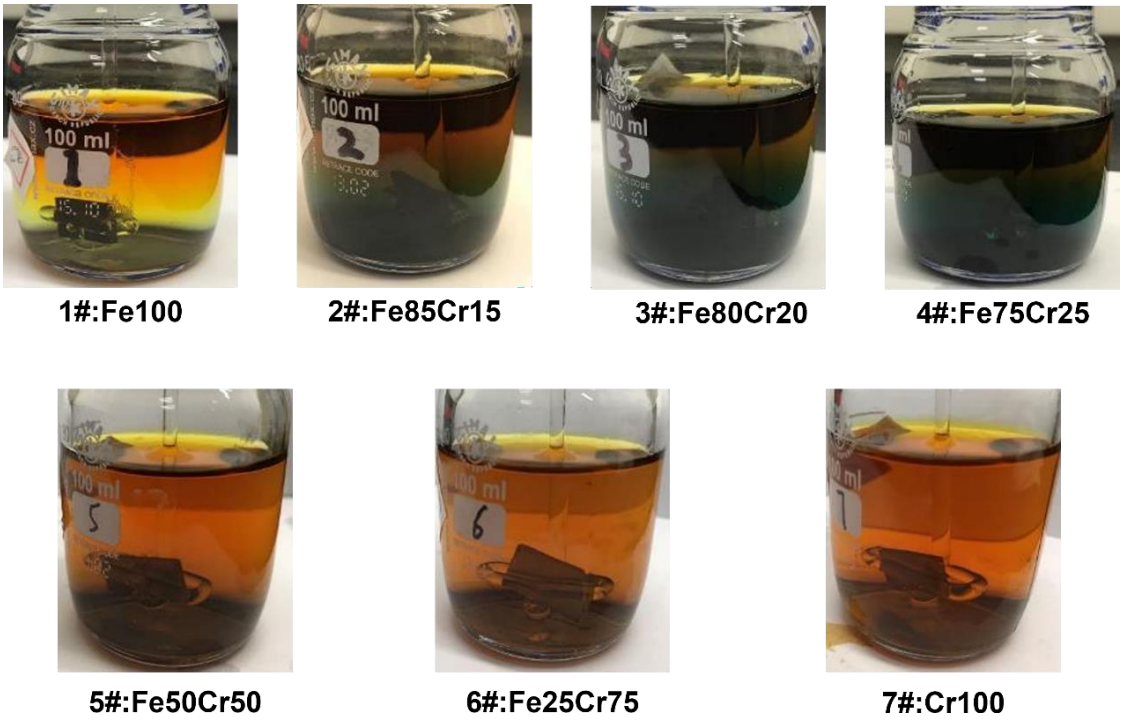

Figure S4. The solution after pitting weight loss test of FeCr alloys in $FeCl_3$.

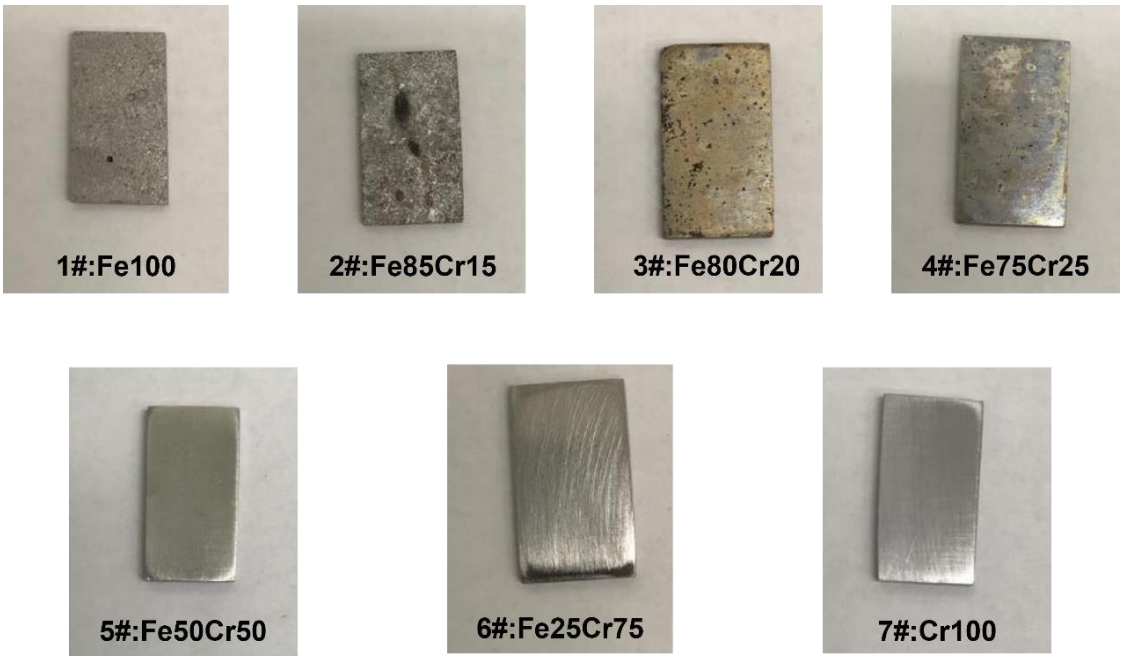

Figure S5. The FeCr alloys after pitting weight loss test in $FeCl_3$

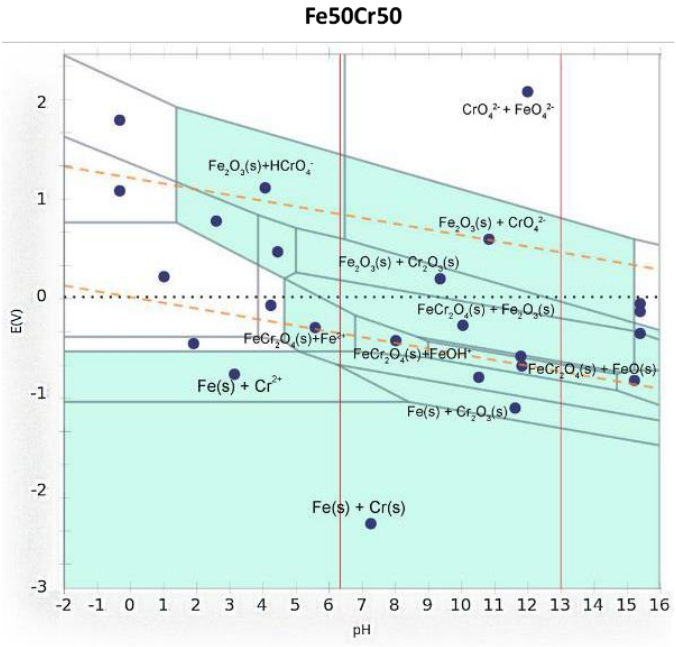

Figure S6. Pourbaix diagram of Fe50Cr50 alloy obtained using the *Materials Project*.

Supporting Tables

Table S1. Summary of onset potentials and limiting currents- forward scan.

Sample	100 rpm			1500 rpm			2500 rpm		
Forward	Onset potential V vs Hg/HgO	Onset potential V vs RHE	Limiting current/ mA	Onset potential V vs Hg/HgO	Onset potential V vs RHE	Limiting current/ mA	Onset potential V vs Hg/HgO/	Onset potential V vs RHE	Limiting current/ mA
Cr100	-0.692	0.240	-0.220	-0.580	0.352	-0.910	-0.553	0.379	-1.118
Fe25Cr75	-0.673	0.259	-0.245	-0.607	0.325	-0.869	-0.426	0.506	-1.257
Fe35Cr65	-0.651	0.281	-0.266	-0.607	0.325	-0.927	-0.536	0.396	-1.267
Fe50Cr50	-0.685	0.247	-0.251	-0.646	0.286	-0.909	-0.516	0.416	-1.266
Fe75Cr25	-0.599	0.333	-0.264	-0.621	0.311	-1.017	-0.634	0.298	-1.045
Fe80Cr20	-0.604	0.328	-0.262	-0.619	0.313	-0.929	-0.626	0.306	-1.172
Fe85Cr15	-0.607	0.325	-0.260	-0.616	0.316	-0.961	-0.626	0.306	-1.170
Fe100	-0.602	0.330	-0.265	-0.587	0.345	-1.083	-0.580	0.352	-1.367

Table S2. Summary of onset potentials and limiting currents- reverse scan.

Sample Reverse	100 rpm			1500 rpm			2500 rpm		
	Onset potential V vs Hg/HgO	Onset potential V vs RHE	Limiting current/ mA	Onset potential V vs Hg/HgO	Onset potential V vs RHE	Limiting current/ mA	Onset potential V vs Hg/HgO/	Onset potential V vs RHE	Limiting current/ mA
Cr100	-0.796	0.136	-0.099	-0.843	0.089	-0.125	-0.865	0.067	-0.126
Fe25Cr75	-0.586	0.346	-0.281	-0.652	0.280	-0.607	-0.662	0.270	-0.641
Fe35Cr65	-0.564	0.368	-0.285	-0.601	0.331	-0.973	-0.620	0.312	-0.974
Fe50Cr50	-0.569	0.363	-0.279	-0.559	0.373	-1.069	-0.584	0.348	-1.306
Fe75Cr25	-0.603	0.329	-0.283	-0.616	0.316	-1.019	-0.620	0.312	-1.269
Fe80Cr20	-0.613	0.319	-0.283	-0.625	0.307	-1.034	-0.630	0.302	-1.315
Fe85Cr15	-0.620	0.312	-0.283	-0.628	0.304	-1.040	-0.630	0.302	-1.328
Fe100	-0.633	0.299	-0.281	-0.633	0.299	-1.073	-0.635	0.297	-1.355

Table S3. Koutecky-Levich analysis of FeCr alloys forward scans (-0.018 V, -0.068 V & -0.118 V vs. RHE; -0.95 V, -1.0 V & -1.05 V vs. Hg/HgO (0.1M NaOH))

Forward	fitting equation	n
Cr100 -0.118 V	y = 9.207 x - 0.0210	2.92
Cr100 -0.068 V	y = 9.428 x - 0.0232	2.86
Cr100 -0.018 V	y = 9.856 x - 0.0294	2.73
Fe25Cr75 -0.268 V	y = 8.112 x + 0.0215	3.32
Fe25Cr75 -0.118 V	y = 8.046 x + 0.0043	3.35
Fe25Cr75 -0.068 V	y = 8.114 x + 0.0043	3.32
Fe25Cr75 -0.018 V	y = 8.306 x + 0.0065	3.24
Fe35Cr65 -0.268 V	y = 7.682 x + 0.0081	3.50
Fe35Cr65 -0.118 V	y = 7.432 x + 0.0176	3.62
Fe35Cr65 -0.068 V	y = 7.522 x + 0.0222	3.58
Fe35Cr65 -0.018 V	y = 7.735 x + 0.0290	3.48
Fe50Cr50 -0.118 V	y = 7.959 x + 0.0020	3.38
Fe50Cr50 -0.068 V	y = 8.230 x + 0.0052	3.27
Fe50Cr50 -0.018 V	y = 8.506 x + 0.0149	3.16
Fe75Cr25 -0.118 V	y = 6.919 x + 0.0292	3.89
Fe75Cr25 -0.068 V	y = 6.914 x + 0.0378	3.89
Fe75Cr25 -0.018 V	y = 6.739 x + 0.0591	3.99
Fe80Cr20 -0.118 V	y = 7.034 x + 0.2280	3.83
Fe80Cr20 -0.068 V	y = 7.032 x + 0.0286	3.83
Fe80Cr20 -0.018 V	y = 6.990 x + 0.0368	3.85
Fe85Cr15 -0.118 V	y = 7.257 x + 0.0123	3.71
Fe85Cr15 -0.068 V	y = 7.187 x + 0.0190	3.75
Fe85Cr15 -0.018 V	y = 7.128 x + 0.0260	3.78
Fe100 -0.118 V	y = 7.557 x - 0.0121	3.56
Fe100 -0.068 V	y = 7.265 x - 0.0051	3.71
Fe100 -0.018 V	y = 7.170 x - 0.0016	3.75

Table S4. Koutecky-Levich analysis of FeCr alloys reverse scans (-0.018 V, -0.068 V & -0.118 V vs. RHE; -0.95 V, -1.0 V & -1.05 V, vs. Hg/HgO (0.1M NaOH))

Reverse	fitting equation	n
Cr100 -0.118 V	-	-
Cr100 -0.068 V	-	-
Cr100 -0.018 V	-	-
Fe25Cr75 -0.368 V	y = 4.874 x + 0.194	5.52
Fe25Cr75 -0.118 V	y = 4.491 x + 0.275	5.99
Fe25Cr75 -0.068 V	y = 4.028 x + 0.314	6.68
Fe25Cr75 -0.018 V	y = 3.421 x + 0.374	7.87
Fe35Cr65 -0.368 V	y = 6.468 x + 0.0404	4.16
Fe35Cr65 -0.118 V	y = 6.520 x + 0.0528	4.13
Fe35Cr65 -0.068 V	y = 6.192 x + 0.0660	4.35
Fe35Cr65 -0.018 V	y = 5.965 x + 0.0856	4.52
Fe50Cr50 -0.118 V	y = 7.090 x + 0.0040	3.80
Fe50Cr50 -0.068 V	y = 6.898 x + 0.0091	3.90
Fe50Cr50 -0.018 V	y = 6.845 x + 0.0139	3.93
Fe75Cr25 -0.118 V	y = 7.016 x + 0.0076	3.84
Fe75Cr25 -0.068 V	y = 6.944 x + 0.0127	3.88
Fe75Cr25 -0.018 V	y = 6.958 x + 0.0178	3.87
Fe80Cr20 -0.118 V	y = 7.021 x + 0.0063	3.83
Fe80Cr20 -0.068 V	y = 6.955 x + 0.0114	3.87
Fe80Cr20 -0.018 V	y = 6.942 x + 0.0175	3.88
Fe85Cr15 -0.118 V	y = 7.219 x + 0.0026	3.73
Fe85Cr15 -0.068 V	y = 7.156 x + 0.0069	3.76
Fe85Cr15 -0.018 V	y = 7.040 x + 0.0157	3.82
Fe100 -0.118 V	y = 7.082 x + 0.0026	3.80
Fe100 -0.068 V	y = 7.013 x + 0.0076	3.84
Fe100 -0.018 V	y = 6.995 x + 0.0161	3.85

Table S5. Summary of solution pitting corrosion in ferric chloride (weight loss test)

Samples	length/mm	Width/ mm	Thickness/mm	Total area /cm^2	Weight loss/ g*	Mass loss corrosion rates / g*cm^{-2}	Rate/ g m^{-2} day^{-1}
Fe100	18.8	10.4	2.2	5.17	0.48146	0.09304	310
Fe85Cr15	18.5	10.9	2.1	5.18	0.50356	0.09722	324
Fe80Cr20	18.9	10.6	2.2	5.32	0.47431	0.08913	297
Fe75Cr25	18.8	10.7	1.7	5.07	0.42064	0.08300	277
Fe50Cr50	19.2	9.8	2.4	5.15	0.01889	0.00367	12.2
Fe25Cr75	19.2	11.5	2.3	5.83	0.00005	0.00001	0.03
Cr100	18.0	9.4	2.2	4.58	0.00010	0.00002	0.07

***Mass loss corrosion rates of greater than or equal to 1 g/cm^2 may be indicative of pitting or crevice corrosion.**